Research Square

Preprints are preliminary reports that have not undergone peer review.
They should not be considered conclusive, used to inform clinical practice,
or referenced by the media as validated information.

Genome-Guided Computational Profiling of Selected Antibiotics for Repurposing against Multiple Resistance Proteins in Multidrug-Resistant Stenotrophomonas maltophilia

Hajar Fauzan Ahmad
fauzanahmad@umpsa.edu.my
Universiti Malaysia Pahang Al-Sultan Abdullah
Md. Shaon Mia
University of Dhaka
Md. Nazim Uddin
Bangladesh Council of Scientific and Industrial Research
Elias Ali
University of Dhaka
Roney Miah
Universiti Malaysia Pahang Al-Sultan Abdullah
Shing Wei Siew
Universiti Malaysia Pahang Al-Sultan Abdullah

Article

Keywords: Stenotrophomonas maltophilia, antibiotic resistance, molecular docking, molecular dynamics simulation, MM/GBSA, resistance-associated proteins

Posted Date: September 2nd, 2026

DOI: https://doi.org/10.21203/rs.3.rs-10763193/v1

License: This work is licensed under a Creative Commons Attribution 4.0 International License. Read Full License

Additional Declarations: No competing interests reported.

Abstract

Background

Stenotrophomonas maltophilia is an intrinsically multidrug-resistant Gram-negative pathogen with a diverse resistome involving antibiotic modification, target alteration, and enzymatic drug inactivation. This study investigated the predicted interactions of selected antibiotics with three resistance-associated proteins, AAC(6')-Ib4, DfrA14, and L1 metallo-β-lactamase from strain CW002SM, with the aim of identifying target-specific interaction patterns and prioritizing candidates for further investigation.

Methods

High-identity comparative models of AAC(6')-Ib4, DfrA14, and L1 metallo-β-lactamase were generated and assessed using GMQE, QMEANDisCo, ERRAT, Ramachandran statistics, and Verify3D. A focused docking panel comprising kanamycin C, trimethoprim, imipenem, and meropenem was evaluated against the principal P2Rank-predicted pocket of each target, while cefiderocol was docked separately as a clinically relevant comparator. Kanamycin C and cefiderocol were subsequently subjected to single 100-ns molecular dynamics (MD) simulations, followed by analyses of ligand and protein RMSD/RMSF, radius of gyration, solvent-accessible surface area, hydrogen bonding, principal component analysis, free-energy landscapes, dynamic cross-correlation, and MM/GBSA energy decomposition.

Results

Kanamycin C achieved the highest within-target docking rank against AAC(6')-Ib4 (− 8.856 kcal/mol), DfrA14 (− 7.719 kcal/mol), and the selected L1 surface pocket (− 5.678 kcal/mol), resulting in a mean cross-target rank of 1.00. MD simulations revealed distinct target-dependent behaviours. Kanamycin C maintained a comparatively stable positional ensemble in AAC(6')-Ib4, whereas cefiderocol underwent progressive reorientation. In DfrA14, kanamycin C displayed multiple positional states, while cefiderocol maintained a comparatively compact ligand ensemble. Both L1 complexes exhibited pronounced late-stage ligand displacement, indicating limited support for a persistent binding geometry at the selected alternative surface pocket. MM/GBSA analysis further supported charge-assisted recognition of kanamycin C by AAC(6')-Ib4 and predominantly van der Waals-driven interactions for cefiderocol with DfrA14.

Conclusion

The integrated computational analysis identified kanamycin C as the most consistent cross-target candidate within the focused docking panel, with AAC(6')-Ib4–kanamycin C showing the strongest convergence among docking, MD, and MM/GBSA observations. The findings provide experimentally testable hypotheses concerning antibiotic–resistance-protein interactions and may guide subsequent investigations of resistance mechanisms, antimicrobial susceptibility, and potential antibiotic-potentiation effects in *S. maltophilia*. Nevertheless, these results represent computational predictions and should not be interpreted as evidence of confirmed target inhibition, resistance reversal, or clinical antibiotic repurposing.

1. Introduction

Antimicrobial resistance (AMR) is a major threat to global health security, undermining the effective treatment of bacterial infections and increasing morbidity, mortality, and healthcare costs. Bacterial AMR is directly responsible for more than one million deaths annually, with millions more deaths associated with resistant infections, and its global burden is

projected to increase substantially in the coming decades without effective interventions [1, 2]. In response to this growing threat, the World Health Organization (WHO) 2024 Bacterial Priority Pathogens List prioritises pathogens and resistance mechanisms requiring urgent research, development, and public-health investment [3]. However, the clinical antibacterial pipeline continues to show limited progress, particularly against multidrug-resistant Gram-negative pathogens, which possess diverse and rapidly evolving resistance mechanisms [4]. Therefore, the urgent development of novel therapeutic strategies and identification of new approaches to overcome bacterial resistance remain critical priorities in addressing the global AMR crisis.

S. maltophilia is an aerobic, non-fermenting, environmentally ubiquitous Gram-negative bacillus that has emerged as an important opportunistic pathogen, particularly among immunocompromised patients, mechanically ventilated individuals, and those with cystic fibrosis [5]. The organism exhibits intrinsic resistance to β-lactams, aminoglycosides, and several other antibiotic classes through β-lactamase production, active efflux, reduced outer-membrane permeability, and target modification or replacement [6]. Comparative genomic studies have revealed substantial diversity and mobility of resistance determinants among clinical and environmental *S. maltophilia* complex isolates [7, 8]. Treatment options remain limited, with trimethoprim-sulfamethoxazole, levofloxacin, and cefiderocol representing important therapeutic options; however, increasing non-susceptibility and the need for combination therapy complicate clinical management [9, 10]. Regulatory networks involving outer-membrane porin expression, σ-factor signalling, and β-lactamase induction further contribute to the complex nature of β-lactam resistance [11, 12]. Comparative analyses of *bla*L1-like determinants across *Stenotrophomonas* species have demonstrated considerable diversity within the L1 metallo-β-lactamase family [13–15]. Clinical studies have reported substantial mortality associated with *S. maltophilia* bacteraemia, while global analyses demonstrate considerable variation in antimicrobial resistance patterns [16–18]. These challenges underscore the need for improved mechanistic understanding and novel resistance-targeted therapeutic strategies [19–21].

The resistance determinants examined in this study represent three complementary mechanisms of antibiotic resistance. AAC(6')-Ib4, an aminoglycoside 6'-N-acetyltransferase, inactivates susceptible aminoglycosides by transferring an acetyl group from acetyl-coenzyme A to the 6'-amino group, thereby reducing productive ribosomal binding [22]. Recent studies have demonstrated the potential of small-molecule adjuvants, including pyrrolidine-pentamine and related chemotypes, to inhibit AAC(6')-Ib enzymes and restore aminoglycoside activity [23–27]. DfrA14 represents a distinct target-replacement mechanism by encoding a trimethoprim-insensitive dihydrofolate reductase that maintains folate metabolism despite antibiotic exposure [28, 29]. Structural and mutational studies have identified conserved features associated with trimethoprim insensitivity and continue to expand understanding of resistance-associated Dfr variants [30–32]. The third determinant, L1 metallo-β-lactamase, is a zinc-dependent B3 subclass enzyme that hydrolyses a broad range of β-lactam antibiotics, including carbapenems [13–15]. Its resistance to clinically available serine-β-lactamase inhibitors further highlights the therapeutic challenge posed by this hydrolytic resistance mechanism.

A focused antibiotic panel was selected to enable both target-specific and cross-target comparisons. Kanamycin C was chosen as an aminoglycoside scaffold relevant to AAC(6')-Ib-type recognition [33], trimethoprim as a mechanistic comparator for resistant DfrA enzymes [28, 30], and imipenem and meropenem as carbapenem comparators for L1 metallo-β-lactamase [14, 15]. Cefiderocol was additionally included as a clinically relevant siderophore cephalosporin used for difficult-to-treat Gram-negative infections, including *S. maltophilia* [9, 10, 34]. Comparative docking and molecular-dynamics analyses can help identify substrate-compatible recognition patterns, potential alternative-pocket interactions, and structural features for subsequent resistance-modulation studies [24, 25, 35]. However, favourable docking scores and persistent simulated poses do not establish physical binding, enzyme inhibition, or antibiotic potentiation. Therefore, computationally prioritised interactions require validation through orthogonal binding assays, enzyme-kinetic studies, and microbiological potentiation experiments [23, 24, 26, 27, 35].

The present study employs an integrated computational framework combining comparative homology modelling, structural validation, binding-pocket prediction, molecular docking, molecular dynamics (MD) simulations, principal

component analysis (PCA), free-energy landscape (FEL) analysis, and Molecular Mechanics/Generalized Born Surface Area (MM/GBSA) analysis to investigate antibiotic recognition by AAC(6')-Ib4, DfrA14, and L1 from *S. maltophilia* CW002SM. The study focuses on identifying and comparing potential interactions of kanamycin C, trimethoprim, imipenem, and meropenem across the resistance-associated targets, with particular emphasis on the cross-target behaviour of kanamycin C. The dynamic stability and energetic characteristics of kanamycin C and cefiderocol were further evaluated using 100-ns MD simulations and MM/GBSA analysis. Overall, this approach was designed to identify reproducible computational interaction patterns and generate experimentally testable hypotheses regarding AMR-protein recognition. Importantly, docking and MM/GBSA results were considered comparative computational evidence rather than direct measures of binding affinity, enzyme inhibition, or antibiotic potentiation [35–37].

2. Materials and Methods

2.1 Study design

This was a computational, structure-based study of three chromosomally encoded resistance determinants from *S. maltophilia* strain CW002SM. The primary score-ranked docking panel comprised four selected antibiotics, namely kanamycin C, trimethoprim, imipenem, and meropenem, which were evaluated against all three targets using the same protein preparation, grid settings, and Glide workflow. Cefiderocol was included separately as a clinically relevant comparator and docked to generate starting complexes for MD simulations. No biochemical inhibition, enzyme-kinetic, or antibacterial susceptibility experiments were performed.

2.2 Sequence translation and target selection

Coding sequences for *aac(6')-Ib4* (555 bp), *dfrA14* (474 bp), and *blaL1* (873 bp) were retrieved from the strain-level genomic and gene dataset of *S. maltophilia* CW002SM(GenBank accession CP104863, BioProject PRJNA876089) and translated in silico using the ExPASy Translate tool. The resulting predicted proteins comprised 179 residues for AAC(6')-Ib4, 157 residues for DfrA14, and 267 residues for the L1 chain A protomer used in subsequent analyses. These three genes were selected to represent complementary resistance mechanisms, including direct antibiotic modification by AAC(6')-Ib4, replacement of an antibiotic-sensitive metabolic target by DfrA14, and hydrolytic antibiotic inactivation by L1, as summarised in Table 1. The identity of each gene was confirmed against the NCBI Reference Gene Sequence database, corresponding to accessions NG_051844.1 (*aac(6')-Ib4*), NG_056035.1 (*dfrA14*), and NG_047509.1 (*blaL1*).

2.3 Homology modelling

Three-dimensional (3D) models of AAC(6')-Ib4, DfrA14, and L1 were generated using SWISS-MODEL with the ProMod3 engine (version 3.6.0) based on high-identity templates [38,39]. AAC(6')-Ib4, DfrA14, and L1 were modelled using PDB entries 2BUE, 7R6G, and 6UAF, respectively, and treated as single chains for subsequent analyses. Model quality was assessed using GMQE and QMEANDisCo scores, while structural plausibility was visually inspected using WinCoot. No additional manual or energy-based structural refinement was performed.

2.4 Structural validation

Model stereochemistry and structural consistency were evaluated using the SAVES v6.1 meta-server, including PROCHECK/Ramachandran analysis, ERRAT, Verify3D, and WHATCHECK, supplemented by visual inspection in WinCoot [40–42]. Ramachandran analysis was reported as the percentage of residues in favoured, allowed, and outlier regions. Verify3D results were reported as the percentage of residues with an averaged 3D-1D compatibility score ≥0.1 when an unambiguous overall value was available. For DfrA14 and L1, only per-residue Verify3D profiles were available; therefore, no overall percentage was reported to avoid inferring or fabricating missing values. The resulting models were

considered well-supported structural hypotheses based on comparative modelling using high-identity templates rather than experimentally determined structures.

2.5 Focused antibiotic-panel construction

The focused antibiotic panel comprised kanamycin C, trimethoprim, imipenem, meropenem, and cefiderocol. Kanamycin C was selected as an aminoglycoside relevant to AAC(6')-Ib4, trimethoprim as the target-relevant antifolate comparator for DfrA14, imipenem and meropenem as carbapenem comparators for L1, and cefiderocol as a clinically relevant siderophore cephalosporin comparator. Kanamycin C, trimethoprim, imipenem, and meropenem formed the primary score-ranked panel, whereas cefiderocol was docked separately using the same receptor grids to generate poses for subsequent molecular dynamics comparison and was not included in the archived score-ranked files. Co-crystal-derived entries in the archived docking output were treated solely as protocol-reference compounds and excluded from the focused antibiotic ranking.

2.6 Pocket prediction

Candidate ligand-binding pockets were predicted for each validated model using P2Rank through the PrankWeb server (version 2.5.1) [43]. The highest-ranked pocket, based on the P2Rank score, probability, and predicted centroid, was selected as the docking-grid centre for each target (Table 3). For L1, the selected pocket was spatially separated from the principal zinc-proximal catalytic centre characteristic of subclass B3 metallo-β-lactamases and was therefore treated as an alternative, exploratory binding site in subsequent docking and molecular dynamics analyses.

2.7 Molecular docking workflow

2.7.1 Protein preparation

The validated homology models of AAC(6')-Ib4, DfrA14, and L1 chain A (Section 2.3) were prepared for molecular docking using the Protein Preparation Wizard in Schrödinger Maestro, following established protein-preparation procedures [44]. The workflow included assignment of bond orders, addition of missing hydrogen atoms, side chains, and short loops, structural refinement using Prime, removal of non-interacting water molecules, generation of appropriate ionization and tautomeric states for hetero groups, optimization of the hydrogen-bonding network, and restrained minimization to a heavy-atom root-mean-square deviation (RMSD) of 0.3 Å using the impref module with the OPLS3e force field [44,45].

2.7.2 Ligand preparation

Kanamycin C, trimethoprim, imipenem, meropenem, and cefiderocol were prepared using LigPrep v3.1 [44,46]. Ligand preparation involved desalting, hydrogen addition, generation of appropriate ionization and tautomeric states using Epik v2.9 at pH 7 ± 0.2, and energy minimization with the OPLS3e force field [45,47]. The lowest-energy prepared state corresponding to the documented docking pose was retained in Maestro format for subsequent interaction analysis and, for kanamycin C and cefiderocol, molecular dynamics (MD) system preparation.

2.7.3 Receptor grid generation and molecular docking

Because the target structures were homology models, receptor grids were independently centred on the highest-ranked P2Rank pocket of each protein (Table 3), with coordinates of X = 12.356, Y = 6.502, Z = 15.909 for AAC(6')-Ib4, X = 16.255, Y = −27.561, Z = 5.941 for DfrA14, and X = 26.209, Y = 45.395, Z = −4.206 for L1 chain A. Kanamycin C, trimethoprim, imipenem, and meropenem were docked into the respective target grids using Glide, with Standard Precision screening followed by Extra Precision docking and rescoring [48,49]. The most favourable archived XP score for each antibiotic was retained for within-target ranking. Cefiderocol was docked separately using the same grids to generate starting poses for subsequent molecular dynamics simulations and was treated as a comparator rather than included in the score-ranked

matrix. Cross-target prioritisation was based on consistency of within-target rankings rather than direct comparison of raw docking scores between different proteins.

2.7.4 Contact analysis

Protein–ligand interactions were evaluated using two distance-based criteria: a general atom-to-atom contact distance of ≤4.0 Å and a stricter protein–ligand nitrogen-to-oxygen (N–O) distance of ≤3.5 Å as a geometric indicator of potential polar interactions. The 3.5 Å N–O criterion was used descriptively and was not considered a formal hydrogen bond because bond-angle geometry was not validated. Docking scores were interpreted as target-specific relative rankings generated by the XP scoring function rather than as experimentally measured binding affinities.

2.8 MD system preparation

Six ligand-bound complexes were subjected to molecular dynamics (MD) simulations: AAC(6')-Ib4–kanamycin C, AAC(6')-Ib4–cefiderocol, DfrA14–kanamycin C, DfrA14-cefiderocol, L1-kanamycin C, and L1-cefiderocol. Kanamycin C was selected because it ranked first within the focused antibiotic panel across all three targets, while cefiderocol was included as a clinically relevant comparator based on separately generated docking poses. Corresponding apo-protein trajectories were used as structural references. Simulations were performed using GROMACS 2023.2 with the CHARMM27 protein force field [50,51]. Ligand parameters and partial charges were generated using the CHARMM General Force Field (CGenFF) [52,53], while each system was explicitly solvated with TIP3P water and neutralised with counterions[54].

2.9 Minimization and equilibration

Each solvated and neutralised system underwent energy minimisation using the steepest-descent algorithm for a maximum of 50,000 steps, followed by sequential equilibration under the NVT ensemble at 300 K and the NPT ensemble at 310 K and 1 bar.

2.10 Production simulation

Production MD simulations were performed for 100 ns per complex using a 2-fs integration time step. A single production trajectory was generated for each ligand-bound complex and corresponding apo system, without independent replicate simulations. This single-trajectory design is explicitly acknowledged as a methodological limitation in Section 3.9.

2.11 Trajectory processing and analysis

Periodic-boundary artefacts were corrected using gmx trjconv, while RMSD, RMSF, radius of gyration (Rg), solvent-accessible surface area (SASA), and hydrogen-bond analyses were performed using standard GROMACS tools. Ligand-bound systems were evaluated using ligand heavy-atom RMSD after protein fitting, whereas apo systems used protein Cα RMSD. Ligand RMSD was further examined in consecutive 20-ns intervals, and protein RMSF was assessed at residue level, particularly around predicted binding pockets. Rg was used to assess structural compactness. SASA and hydrogen-bond analyses were interpreted conservatively because the original index selections and residue-resolved occupancy data were unavailable.

2.12 Principal component analysis (PCA) and free-energy landscape (FEL) analysis

Principal component analysis (PCA) was performed to characterise essential protein motions in both ligand-bound and apo trajectories [55]. Following least-squares fitting to the protein backbone, Cα covariance matrices were generated using gmx covar and diagonalised to obtain the corresponding eigenvalues and eigenvectors. PC1–PC2 projections were generated using gmx anaeig, and the percentage contribution of each principal component to the total variance was calculated from its eigenvalue relative to the sum of all eigenvalues. Free-energy landscapes (FELs) were constructed from the PC1–PC2 projections using gmx sham [56] and interpreted descriptively based on the distribution, separation,

and connectivity of populated conformational regions. Dynamic cross-correlation maps (DCCMs) were also examined qualitatively to compare correlated and anticorrelated residue motions between the kanamycin C and cefiderocol systems. As each system was represented by a single trajectory and the underlying covariance and correlation matrices were not retained, PCA, FEL, and DCCM results were interpreted as qualitative descriptors rather than statistically replicated or fully converged thermodynamic properties.

2.13 MM/GBSA and per-residue decomposition

End-state binding free-energy calculations were performed using gmx_MMPBSA version 1.6.3, based on the MMPBSA.py v16.0 framework, with the Generalized Born (GB) implicit-solvent model [36,57,58]. The nonpolar contribution was estimated using the LCPO-based solvent-accessible surface area (SASA) approach. Per-residue energy decomposition was performed using idecomp = 2 to obtain total, sidechain, and backbone energetic contributions. Calculations were conducted at 298.15 K using 100 representative frames extracted from each 100-ns trajectory, without an entropy correction. The binding free energy was estimated as:

$\Delta G_{bind} = \Delta E_{vdW} + \Delta E_{electrostatic} + \Delta G_{GB} + \Delta G_{nonpolar}$

The resulting MM/GBSA values were interpreted as comparative, target- and ligand-specific end-state interaction-energy estimates rather than experimentally measured thermodynamic binding affinities. Similarly, per-residue decomposition values were considered computed energetic contributions and were not interpreted as experimentally determined residue-level affinities. For the L1-kanamycin C complex, the corrected independently rerun MM/GBSA dataset (KANAMYCIN_beta_1 archive) was used instead of the originally archived L1–kanamycin dataset. The original L1 MM/GBSA output corresponded to the L1-cefiderocol complex, and this assignment was verified against the primary .dat and .csv output files before values were incorporated into the manuscript.

3. Results and Discussion

3.1 Model construction and validation

Homology modeling is an important component of structure-based antibacterial drug discovery, particularly for bacterial targets whose experimentally determined three-dimensional structures are unavailable. By generating reliable protein structures from homologous templates, homology modeling provides structural information on active sites, binding pockets, and key residues required for rational ligand design and molecular docking [59,60]. These predicted structures can subsequently support virtual screening, docking, binding-mode analysis, and lead optimization, thereby reducing the time and cost associated with experimental screening [60,61]. Because the emergence of multidrug-resistant bacteria has intensified the need for novel antibacterial agents, integrating homology modeling with structure-based approaches can facilitate the identification and prioritization of potential inhibitors against previously underexplored bacterial resistance-associated and essential proteins [62,63].

Comparative structural models of AAC(6')-Ib4, DfrA14, and L1 chain A were generated using templates exhibiting 89.8-99.0% sequence identity to the corresponding target proteins (Table 1). The models demonstrated consistently high GMQE values (0.84–0.92) and QMEANDisCo scores (0.87–0.91), indicating good overall model reliability (Table 2). The ERRAT quality factors were 96.364 for AAC(6')-Ib4, 84.173 for DfrA14, and 92.948 for L1. Ramachandran analysis further showed that 98.87%, 92.26%, and 95.66% of residues occupied the preferred regions for AAC(6')-Ib4, DfrA14, and L1, respectively. For AAC(6')-Ib4, 91.62% of residues had averaged Verify3D scores ≥0.1. Although per-residue Verify3D profiles were available for DfrA14 and L1, the archived outputs did not provide an unambiguous single summary percentage. Overall, the high template sequence identity and favorable GMQE, QMEANDisCo, ERRAT, Ramachandran, and Verify3D assessments collectively support the structural reliability of the generated models for comparative binding-pocket analysis, molecular docking, and molecular dynamics simulations (Figure 1; Supplementary Figure S1).

The quality indices obtained for the three comparative models are consistent with the benchmarks generally used to judge SWISS-MODEL-derived structures: GMQE and QMEANDisCo global scores above 0.6 are typically regarded as indicative of reliable models, and templates sharing more than 40% sequence identity with the target commonly yield models with a global Cα RMSD close to 2 Å relative to the corresponding experimental structure [38,39]. Because the AAC(6')-Ib4, DfrA14, and L1 templates used here shared 89.8–99.0% sequence identity with the target proteins, the resulting GMQE (0.84–0.92) and QMEANDisCo (0.87–0.91) values, together with the ERRAT, Ramachandran, and Verify3D outputs, fall within or above the ranges generally reported as acceptable for structure-based docking and molecular dynamics applications, supporting the use of these models for the subsequent pocket, docking, and dynamics analyses.

3.2 Pocket architecture

P2Rank/PrankWeb identified a single dominant, high-confidence binding pocket in each target protein (Table 3). Among the three targets, the DfrA14 pocket exhibited the highest P2Rank probability (0.989) and score (66.29), consistent with the well-defined and evolutionarily conserved dihydrofolate-binding cleft characteristic of dihydrofolate reductase (DHFR) folds. The principal pocket residues, including Met9, Ala10, Ala11, Ile18, Trp26, Glu31, Gln32, Phe35, Thr50, Met54, Leu57, Ser100, Gly102, and Tyr106, form a combination of polar anchoring sites and an extended hydrophobic wall. The AAC(6')-Ib4 pocket showed a high P2Rank probability (0.979) and score (52.01) and was characterized by an acidic residue cluster comprising Asp126, Asp163, and Asp190, flanked by polar residues (Gln75, Gln102, Ser109, and Asn168) and aromatic residues (Tyr104 and Trp113). This electrostatic and structural environment is consistent with recognition of the polycationic aminoglycoside scaffold. In contrast, the L1 pocket exhibited a lower P2Rank score (17.74) and probability (0.806) than those of DfrA14 and AAC(6')-Ib4. The predicted L1 pocket was spatially distinct from the canonical zinc-proximal catalytic groove of subclass B3 metallo-β-lactamases and comprised Asn128, Ala129, Glu130, Asp162, Phe177, Pro179, Pro183, Tyr220, Arg222, Asp226, and Arg229, generating a mixed chemical environment containing acidic and basic residues together with proline-flanked aromatic features.

Comparison of the three predicted pockets highlights substantial differences in their structural and physicochemical architectures, while also demonstrating their suitability for interrogation using a common ligand library. The DfrA14 pocket is embedded within a compact and well-packed DHFR fold and exhibited the highest P2Rank confidence metrics among the three targets, consistent with its established role as the physiological folate/antifolate-binding site. The AAC(6')-Ib4 pocket, located within the GNAT-fold acetyltransferase core, displayed a comparatively compact and electronegative environment, consistent with its function in recognizing the polycationic amino-sugar moieties of aminoglycoside substrates. By contrast, the predicted L1 pocket represents a relatively shallow and solvent-exposed surface region within the larger β-lactamase fold. Its lower P2Rank score and probability are consistent with a potentially more dynamically accessible binding environment, in agreement with the greater conformational flexibility subsequently observed for L1 during molecular dynamics simulations (Section 3.4).

Overall, the predicted pockets represent a structural progression from a deep, high-confidence catalytic-adjacent cleft in DfrA14, through a moderately high-confidence, charge-dominated modification-enzyme pocket in AAC(6')-Ib4, to a shallower and potentially more dynamically accessible surface pocket in L1. These differences provide important structural context for interpreting the distinct docking-score ranges and MM/GBSA energy profiles presented in the subsequent sections. Because the three binding pockets differ substantially in size, electrostatic character, and conformational accessibility, docking scores and MM/GBSA energies are not directly compared across targets in absolute terms. The corresponding structural models and predicted binding-pocket representations are presented in Figure 1.

3.3 Focused antibiotic docking and cross-target ranking

Molecular docking is an important structure-based drug discovery technique that predicts the binding orientation and potential interactions of small molecules within the active or binding site of a target protein, thereby providing insights into ligand–target recognition at the molecular level [64,65]. By enabling the rapid computational screening and prioritization of large chemical libraries, molecular docking can reduce the number of compounds requiring experimental testing and thereby improve the efficiency and cost-effectiveness of early-stage hit identification [66,67]. Docking also facilitates the analysis of key interactions, including hydrogen bonds, hydrophobic contacts, and electrostatic interactions, which can guide the rational optimization of promising hits into more potent lead compounds [64,68]. Consequently, docking-based virtual screening has become a widely used component of modern structure-based drug discovery, although its predictions should be experimentally validated because docking scores and scoring functions have recognized limitations [69,70].

The focused, score-ranked docking panel showed a clear within-target ranking of the selected antibiotics across AAC(6')-Ib4, DfrA14, and L1 (Table 4). For AAC(6')-Ib4, kanamycin C exhibited the most favourable docking score (−8.856), followed by imipenem (−7.159), trimethoprim (−5.888), and meropenem (−5.798). Kanamycin C established an extensive polar interaction network within the acidic binding pocket, involving Asp126, Asp163, Glu64, and Asp190, as well as Gln75, Gln102, Tyr104, Trp59, and Trp113. Imipenem occupied the same predicted cavity but formed fewer interactions, consistent with its less favourable docking score.

For DfrA14, kanamycin C again ranked first among the selected antibiotics, with a docking score of −7.719, followed by meropenem (−7.493), trimethoprim (−7.347), and imipenem (−6.900). Trimethoprim occupied the predicted folate/antifolate-binding region and interacted with residues within an overlapping pocket, including Glu31, Met9, Ala10, Ala11, Phe35, Met54, Leu57, and Thr50. The relatively narrow score distribution among kanamycin C, meropenem, and trimethoprim suggests that the compact DfrA14 binding cleft can accommodate chemically diverse antibiotic scaffolds. For subsequent molecular dynamics simulations, kanamycin C and cefiderocol were selected for comparative analysis rather than subjecting the entire docking panel to MD simulation.

At the selected L1 surface pocket, kanamycin C also achieved the most favourable docking score (−5.678), followed by imipenem (−5.524), meropenem (−4.086), and trimethoprim (−3.930). Kanamycin C interacted with Glu130, Pro183, Asp226, Arg137, Arg219, and Arg229. Meropenem contacted Glu130, Arg229, Asp162, Thr233, Phe177, Pro179, and Pro183, whereas imipenem occupied the same alternative surface region. The comparable placement of the two carbapenems within this pocket provides a target-relevant basis for comparison; however, this site is spatially distinct from the experimentally established binuclear zinc catalytic centre of L1. Overall, cross-target prioritisation based on within-target ranking consistently identified kanamycin C as the leading candidate, with a mean rank of 1.00 across all three targets. Imipenem, meropenem, and trimethoprim showed mean ranks of 2.67, 3.00, and 3.33, respectively. Thus, kanamycin C demonstrated the highest and most consistent computational ranking across the focused antibiotic panel. Cefiderocol interaction maps were generated from the separately docked starting poses used for the MD simulations and were therefore excluded from the score-based ranking. Representative interaction profiles are presented in Figure 2, while the complete focused docking score matrix is provided in Supplementary Table S1.

The docking behaviour observed for kanamycin C is broadly consistent with previous structural and computational work on AAC(6')-type acetyltransferases. Crystallographic and Glide-based docking studies of AAC(6')-Ib have shown that its aminoglycoside-binding pocket is shallow and markedly electronegative, with an active-site aspartate positioned to accept a proton from the substrate 6'-amino group, and docking against this pocket has previously been used to rank and prioritise both substrates and small-molecule inhibitors [33,71]. The acidic, polar interaction network identified here for kanamycin C at Asp126, Asp163, Glu64, and Asp190 parallels this established recognition mode. For DfrA14, the ranking of trimethoprim and its interactions with Met9, Ala10, Ala11, Phe35, Met54, Leu57, and Thr50 are consistent with

structural studies of plasmid-encoded DfrA-family dihydrofolate reductases, which identify an equivalent Met20-loop-like region (approximately residues 9–23) and hydrophobic wall as principal determinants of antifolate binding and trimethoprim resistance [30]. At L1, the docking scores obtained for the carbapenems and kanamycin C at the selected surface pocket are comparable in magnitude to, but slightly less favourable than, the −8.1 to −7.2 kcal/mol range reported for high-throughput virtual-screening hits against the same target in an independent in silico and in vitro study, suggesting that the present focused panel did not identify equally high-affinity ligands at this particular site [72].

3.4 MD simulation

MD simulations are an important computational approach in modern drug discovery because they capture the time-dependent flexibility and conformational behavior of proteins and protein–ligand complexes beyond the static structures used in molecular docking [73,74]. MD simulations can therefore assess the structural stability of docked complexes and provide detailed insights into ligand-target interactions, conformational changes, and binding mechanisms at the atomic level [75,76]. Furthermore, MD trajectories can be coupled with binding free-energy calculations to estimate ligand affinities and support the prioritization and optimization of promising drug candidates [77,78]. Thus, integrating MD simulations with molecular docking provides a more comprehensive evaluation of protein-ligand recognition and can strengthen computational workflows for rational drug design [79,80].

3.4 Time-resolved ligand positional behaviour

The ligand-bound and apo trajectories were evaluated using distinct RMSD observables. For the ligand-bound complexes, ligand heavy-atom RMSD was calculated after fitting the protein backbone, whereas protein Cα RMSD was used for the apo proteins. Accordingly, the ligand RMSD profiles were used to evaluate ligand pose retention and displacement, while the apo protein RMSD profiles served as reference measures of intrinsic protein structural behaviour (Figure 3; Table 5; Supplementary Table S3).

The AAC(6')-Ib4–kanamycin C complex exhibited the most stable ligand trajectory. Its mean ligand RMSD values across successive 20-ns intervals were 0.109, 0.191, 0.171, 0.178, and 0.150 nm, indicating a minor initial adjustment followed by a relatively stable positional ensemble. In contrast, cefiderocol showed a progressive increase in RMSD, with block means rising from 0.311 and 0.420 nm during the first 40 ns to 0.649, 0.684, and 0.695 nm over the subsequent 60 ns. The sustained increase without recovery toward the initial RMSD suggests progressive reorientation and displacement from the starting pose rather than transient fluctuations around stable binding geometry.

DfrA14 showed an opposite pattern of ligand retention. Cefiderocol maintained a relatively narrow RMSD range throughout the simulation, with 20-ns block means between 0.154 and 0.187 nm, indicating strong retention of its initial positional state. Kanamycin C, in contrast, displayed greater positional variability, with RMSD means increasing from 0.540 nm during 0–20 ns to 0.740 and 0.853 nm during 20–60 ns, followed by decreases to 0.715 and 0.536 nm during 60–100 ns. This non-monotonic behaviour suggests sampling of alternative ligand orientations or pocket subregions, followed by partial recovery toward a less-displaced state, rather than continuous displacement from the binding site.

The L1 complexes exhibited substantially greater ligand displacement, particularly during the later stages of the simulations. Kanamycin C maintained RMSD values of approximately 0.77–0.85 nm during the first 80 ns but increased sharply to a mean of 4.106 nm during the final 20 ns. Cefiderocol exhibited greater displacement from the beginning, with its block mean increasing from 1.246 nm during 0–20 ns to 2.120–2.134 nm during 40–80 ns and reaching 3.672 nm during 80–100 ns. These pronounced late-stage increases indicate substantial reorganisation of the ligand–protein surface relationship and suggest that neither ligand maintained a single persistent binding geometry at the selected L1 surface pocket throughout the simulation.

The stable ligand-RMSD trajectory obtained for AAC(6')-Ib4–kanamycin C (block means of 0.11–0.19 nm) is consistent with the sub-0.2 nm ligand RMSD generally reported for well-accommodated ligands in comparable resistance-protein docking/MD studies, whereas the progressive rise observed for cefiderocol in this target parallels the late-stage reorientation described for several repurposed drug candidates docked against structurally related enzymes, in which initially favourable poses were not always maintained across the full trajectory [81]. The pronounced late-stage displacement of both ligands at the selected L1 surface pocket (reaching means of 3.7–4.1 nm during the final 20 ns) is substantially larger than the RMSD values reported for compounds docked into the catalytic region of L1 in a recent combined in silico/in vitro study of the same target, in which candidates selected for 300-ns simulation maintained comparatively stable positional behaviour [72]. This contrast supports the interpretation that the alternative surface site investigated here, rather than the canonical zinc-proximal catalytic groove, underlies the limited positional stability observed for L1.

3.5 Protein flexibility, compactness, solvent exposure, and hydrogen-bond dynamics

AAC(6')-Ib4 maintained a compact and comparatively stable protein profile across all three simulation systems. The mean protein RMSF values were 0.119 nm for the kanamycin C complex, 0.127 nm for the cefiderocol complex, and 0.095 nm for the apo protein. The core pocket residues Asp126 and Asp163 remained among the least mobile residues in both ligand-bound systems. However, cefiderocol was associated with greater fluctuations around Glu64 and Trp113 than kanamycin C, consistent with the progressive increase in cefiderocol ligand RMSD and the distinct residue-level energy contributions identified by MM/GBSA analysis. The mean Rg values were 1.578, 1.605, and 1.589 nm for the kanamycin C, cefiderocol, and apo systems, respectively, indicating only minor differences in overall protein compactness. Similarly, the selected-group SASA was lowest for the kanamycin C system (99.31 ± 1.82 nm²), compared with cefiderocol (102.27 ± 2.17 nm²) and the apo system (103.91 ± 1.89 nm²). Kanamycin C maintained a relatively dense hydrogen-bonding network, generally comprising approximately 4–9 contacts throughout the trajectory. In contrast, cefiderocol exhibited a marked reduction in hydrogen bonding at approximately 20–40 ns, followed by partial recovery to a fluctuating range of 3–6 contacts.

DfrA14 exhibited ligand-dependent flexibility primarily around the folate-binding pocket. The mean protein RMSF values were 0.134 nm for kanamycin C, 0.116 nm for cefiderocol, and 0.086 nm for the apo protein. Kanamycin C was associated with increased fluctuations in residues 22–35, particularly Trp26, Glu31, Gln32, and Phe35, whereas this region remained comparatively more restrained in the cefiderocol complex. This residue-level behaviour is consistent with the multiple RMSD plateaus observed for kanamycin C and the comparatively narrow RMSD distribution of cefiderocol. The mean Rg values were 1.567 nm for kanamycin C, 1.542 nm for cefiderocol, and 1.520 nm for apo DfrA14, indicating modest differences in overall compactness. The corresponding selected-group SASA values were 91.62 ± 1.79, 87.73 ± 1.71, and 91.46 ± 1.59 nm², respectively. The lower SASA observed for the cefiderocol-associated system indicates a more compact and less solvent-exposed selected group; however, these values should not be interpreted as direct measures of ligand-specific solvent burial. Hydrogen bonding remained moderate throughout the simulations. Kanamycin C generally maintained approximately 2–5 contacts, with the number decreasing toward approximately 2–4 contacts during the later stages, whereas cefiderocol generally retained 1–5 contacts without a prolonged zero-contact period.

L1 displayed substantially greater global structural mobility than AAC(6')-Ib4 and DfrA14. The mean protein RMSF values were 0.880 nm for kanamycin C, 1.431 nm for cefiderocol, and 1.420 nm for the apo protein, indicating pronounced flexibility in both ligand-bound and apo states. The Rg profiles also showed substantial expansion events, with mean values of 2.849, 2.956, and 2.948 nm for the kanamycin C, cefiderocol, and apo systems, respectively. Notably, the cefiderocol and apo trajectories exhibited late-stage excursions approaching approximately 4–5 nm, indicating substantial changes in global dimensions. The selected-group SASA values were correspondingly high at 238.08 ± 2.99, 236.27 ± 4.70, and 233.29 ± 4.16 nm² for kanamycin C, cefiderocol, and apo L1, respectively. Hydrogen-bond formation did not prevent the pronounced ligand displacement observed at this surface site. Kanamycin C increased from approximately 2–4 contacts during the early stages to 4–7 contacts later in the trajectory, whereas cefiderocol progressed from a sparse initial hydrogen-bonding network to approximately 2–5 contacts after the midpoint of the simulation. These results indicate that hydrogen-bond abundance alone was insufficient to predict ligand retention at the highly dynamic L1 surface site.

The comparatively low protein RMSF (0.095–0.134 nm) and Rg values (1.52–1.61 nm) obtained for AAC(6')-Ib4 and DfrA14 are consistent with the compact, well-packed folds typically reported for GNAT-family acetyltransferases and DHFR-fold proteins in comparable MD studies, in which core secondary-structure elements remain rigid while loop regions accommodate ligand-dependent fluctuations [30,33]. In contrast, the substantially higher RMSF (0.88–1.43 nm) and Rg excursions observed for L1 exceed the flexibility generally reported for compact, single-domain β-lactamases and are more consistent with the greater conformational mobility described for larger or less-constrained metallo-β-lactamase constructs in other computational studies, underscoring that the simulated single-chain L1 model used here does not reproduce the more restrained behaviour expected for the natively assembled, metal-loaded enzyme [82,83]. The hydrogen-bonding trends observed for AAC(6')-Ib4 and DfrA14 also parallel previous reports that stable aminoglycoside or antifolate binding is generally accompanied by a persistent, multi-contact hydrogen-bond network rather than a fixed bond count [71].

3.6 Principal motions, free-energy landscapes, and dynamic cross-correlation

Principal component analysis (PCA) is widely used to reduce the high-dimensional data generated by molecular dynamics simulations and identify the dominant collective motions and conformational changes of protein–ligand complexes, providing insights into ligand-induced structural dynamics relevant to drug discovery [84,85]. Free-energy landscape (FEL) analysis complements PCA by mapping the relative free-energy distribution of sampled conformational states, enabling identification of stable and metastable states and assessment of conformational preferences induced by ligand binding [85,86]. Dynamic cross-correlation matrix (DCCM) analysis further characterizes correlated and anticorrelated motions between residues, helping reveal communication pathways, allosteric effects, and changes in collective protein dynamics upon ligand binding [87,88]. Collectively, PCA, FEL, and DCCM provide complementary dynamic information that can strengthen the interpretation of MD simulations and support the mechanistic evaluation and prioritization of potential drug candidates [80,89].

The conformational landscape analysis further revealed distinct dynamic behaviours among the three protein–ligand systems. For AAC(6')-Ib4–kanamycin C, PC1 and PC2 accounted for 30.28% and 9.94% of the total variance, respectively, while the FEL exhibited an elongated, interconnected low-energy region. This distribution suggests relatively continuous

sampling within a dominant conformational ensemble, consistent with the restrained ligand RMSD profile. In contrast, AAC(6')-Ib4–cefiderocol showed PC1 and PC2 contributions of 21.17% and 12.58%, respectively, with several spatially separated FEL minima, supporting the progressive ligand reorientation observed during the trajectory. The DCCM profiles of both systems were characterized mainly by localized correlated and anticorrelated motions. However, the cefiderocol complex exhibited greater heterogeneity in the off-diagonal regions, indicating altered coordination among residue motions rather than disruption of the overall protein fold.

For DfrA14, the first two principal components explained 50.58% and 40.72% of the total variance for the kanamycin C and cefiderocol complexes, respectively. The FEL of the kanamycin C system displayed multiple distinct low-energy minima, corresponding well with the multiple ligand RMSD plateaus and enhanced flexibility detected within the binding-pocket region. Conversely, cefiderocol sampled a more continuous and concentrated conformational region, consistent with its relatively low and stable ligand RMSD. The DCCM analysis also revealed ligand-dependent differences in the dynamic coupling of the folate-binding region. Kanamycin C produced more pronounced localized changes in correlated motions, whereas cefiderocol maintained a more dispersed pattern of weaker local correlations.

In contrast, the L1 complexes exhibited substantially broader conformational dynamics. PC1 and PC2 together explained more than 95% of the total variance in both ligand-bound trajectories, indicating that the observed structural fluctuations were largely governed by a small number of high-amplitude collective motions. The FELs contained several widely separated populated regions rather than a single dominant low-energy basin, while the DCCM maps revealed extensive regions of both positive and negative correlations. These findings correspond with the substantial Rg fluctuations and pronounced late-stage ligand displacement observed for L1, suggesting considerable global conformational rearrangement of the simulated receptor construct. Nevertheless, in the absence of independent simulation replicates and the underlying numerical correlation matrices, these PCA, FEL, and DCCM findings should be regarded as qualitative evidence of altered collective dynamics rather than conclusive evidence for a specific allosteric mechanism (Figure 4; Supplementary Figure S5).

The narrow, interconnected free-energy landscape and dominant low-percentage PC1/PC2 contributions obtained for AAC(6')-Ib4–kanamycin C are consistent with the single-basin conformational behaviour reported for stably bound ligands in other PCA/FEL-based analyses of resistance-associated enzymes, whereas the multiple FEL minima observed for DfrA14–kanamycin C resemble the multi-basin landscapes described when a ligand samples several sub-pocket orientations rather than a single dominant pose [30]. The markedly higher combined PC1–PC2 variance (>95%) and multiple widely separated FEL minima obtained for both L1 complexes considerably exceed the variance contributions typically reported for compact, single-domain drug targets and are more comparable to the broad collective motions and dispersed correlation patterns described for larger, more flexible enzyme constructs in comparable AMR-protein PCA/FEL/DCCM studies, supporting the interpretation that L1 in this simulation setup underwent substantially greater global conformational rearrangement than the other two targets [81].

3.7 MM/GBSA and per-residue energetic determinants

MM/GBSA is an important end-point free-energy approach in structure-based drug discovery because it estimates protein–ligand binding free energies by combining molecular-mechanics energies with generalized Born solvation and solvent-accessible surface-area terms [90,91]. Compared with conventional molecular-docking scoring functions, MM/GBSA can provide a more physically informed estimation of binding affinity while remaining substantially less computationally demanding than rigorous alchemical free-energy methods [90,92]. When applied to molecular-dynamics trajectories, MM/GBSA can account for conformational ensembles and help-rank candidate ligands according to their relative binding strengths, supporting hit prioritization and lead optimization [93,94]. In addition, MM/GBSA energy decomposition can identify residues and energetic contributions that are important for ligand recognition, providing mechanistic information useful for rational drug design [77,95].

MM/GBSA end-state analysis (Table 6) identified AAC(6')-Ib4–kanamycin C as the most energetically favourable complex, with a total binding free-energy estimate of −78.31 ± 9.55 kcal/mol. This favourable value was primarily associated with strong electrostatic interactions (−1657.96 kcal/mol), which were substantially counterbalanced by an unfavourable polar desolvation contribution (+1608.60 kcal/mol). Additional favourable contributions arose from van der Waals interactions (−23.14 kcal/mol) and nonpolar solvation (−5.81 kcal/mol). Residue-wise decomposition identified Asp163 (−28.68 kcal/mol), Asp126 (−18.82 kcal/mol), and Trp113 (−6.87 kcal/mol) as the major favourable contributors, with additional favourable contributions from Glu64, Tyr104, Gln75, Asp190, and Pro164. The correspondence between these energetic contributors and the docking interaction profile, low ligand RMSD, limited mobility of the acidic-pocket residues, and persistent hydrogen-bonding network supports a coherent charge-assisted recognition mode for kanamycin C. This interpretation is also compatible with recent cellular studies demonstrating the contribution of AAC(6')-Ib abundance to aminoglycoside resistance, together with structural and medicinal-chemistry investigations supporting aminoglycoside recognition and acetyltransferase inhibition as potential approaches for resistance modulation [22,24,27,33]. In contrast, cefiderocol showed a substantially less favourable total estimate of −12.21 ± 8.78 kcal/mol. Asp163 and Asp126 contributed unfavourably, whereas Trp60, Tyr104, Trp113, Gly61, Gly62, Ser109, and Pro164 provided the principal favourable contributions. This redistribution of residue-level energetics is consistent with the progressive reorientation of cefiderocol observed during the MD trajectory.

For DfrA14, the cefiderocol complex showed a more favourable MM/GBSA estimate than the kanamycin C complex (−25.25 ± 5.06 versus −15.43 ± 8.18 kcal/mol). The cefiderocol energy profile was dominated by favourable van der Waals interactions (−70.63 kcal/mol) and exhibited the most favourable nonpolar-solvation contribution among the six simulated complexes (−9.05 kcal/mol). Met54, Phe35, Leu57, Ile18, Thr50, Gln32, and Ser100 were the principal favourable residue contributors. These interactions, together with the low ligand RMSD and restrained flexibility of the pocket region, suggest stable engagement with the hydrophobic wall of the folate-binding cleft. This behaviour is compatible with structural studies of plasmid-encoded DfrA enzymes showing that active-site substitutions and changes in ligand–cofactor cooperativity can modify trimethoprim recognition while maintaining the overall DHFR fold [30]. Furthermore, recent broad mutational-scanning studies indicate that DHFR homologues can tolerate substantial sequence variation while exhibiting heterogeneous inhibitor responses [96]. n comparison, kanamycin C showed favourable contributions from Ser53, Ile24, Trp26, Pro22, Asp23, Ala28, Met54, and Gly21, but was associated with greater pocket-region flexibility and positional switching. Collectively, these findings suggest distinct recognition behaviours, with cefiderocol forming a comparatively compact, van der Waals-dominated interaction ensemble and kanamycin C exhibiting a more conformationally mobile binding mode.

At L1, the corrected MM/GBSA estimate for kanamycin C was −23.16 ± 12.01 kcal/mol, compared with −12.77 ± 5.61 kcal/mol for cefiderocol. Kanamycin C exhibited strong electrostatic attraction (−611.37 kcal/mol), which was largely offset by an unfavourable polar desolvation contribution (+598.02 kcal/mol). The principal favourable residue contributions arose from Asp226, Glu225, Glu130, and Pro221. For cefiderocol, Leu143, Arg219, Pro218, Asn141, Asp142, and Tyr220 were the major favourable contributors. Structural studies of product-bound and time-resolved L1 complexes have established that β-lactam recognition and hydrolysis occur at the binuclear zinc catalytic centre, with conserved substrate and product interactions within this region [15,82]. Therefore, the present energetics at the selected surface pocket should not be interpreted as evidence of catalytic-site inhibition. Although the MM/GBSA values describe favourable interactions sampled during the trajectories, they do not negate the pronounced late-stage ligand displacement, substantial Rg excursions, and broad collective motions observed for L1. Accordingly, the L1 energetic results are considered contact-level hypotheses for an alternative surface site within a highly dynamic system rather than evidence of a stable high-affinity complex. The component energy profiles are presented in Figure 5, while the residue-level decomposition is provided in Supplementary Figure S4.

The strongly favourable, electrostatically dominated MM/GBSA estimate obtained for AAC(6')-Ib4–kanamycin C (−78.31 ± 9.55 kcal/mol) is considerably more negative than the total binding free energies typically reported for small-molecule

ligands and inhibitors of related aminoglycoside-modifying enzymes and metallo-β-lactamases in comparable end-state MM/GBSA studies [72,81]; this magnitude reflects the large, mutually compensating electrostatic and polar-desolvation terms characteristic of a highly charged aminoglycoside engaging an acidic pocket, rather than necessarily indicating a proportionally stronger true binding affinity. The more moderate estimates obtained for DfrA14–cefiderocol (−25.25 ± 5.06 kcal/mol) and the L1 complexes (−23.16 and −12.77 kcal/mol) fall within the range reported for other computationally screened ligands against related resistance-associated targets, including the docking range and corresponding MD-derived stability reported for candidate inhibitors of L1 from S. maltophilia in an independent study [72], supporting the relative, within-target interpretation of these values adopted throughout the present work.

3.8 Integrated mechanistic interpretation and antibiotic prioritisation

The focused docking-panel analysis yielded one consistent cross-target finding: kanamycin C ranked first within each of the three predicted binding sites. This prioritisation was based on consistency of within-target ranking rather than direct comparison of absolute docking scores between structurally distinct proteins [35,97]. However, the subsequent MD simulations demonstrated that a favourable docking rank did not necessarily correspond to equivalent ligand stability or binding behaviour across the different targets.

AAC(6')-Ib4 provided the strongest and most internally consistent computational evidence for kanamycin C recognition. The persistent ligand pose, sustained hydrogen-bonding network, low mobility of the key acidic-pocket residues Asp126 and Asp163, and strongly electrostatic MM/GBSA profile collectively support a stable charge-assisted recognition mode. Within this framework, kanamycin C serves as a structurally relevant aminoglycoside benchmark, while its consistent cross-target ranking provides a rationale for further investigation of potential resistance-modulating activity.

For DfrA14, kanamycin C achieved the highest docking rank but subsequently displayed considerable positional switching and increased flexibility around residues forming the folate-binding region. Conversely, cefiderocol, which was introduced as a separately docked comparator for the MD analysis, maintained a more compact conformational ensemble and exhibited a more favourable van der Waals-dominated MM/GBSA profile. This contrast highlights the importance of integrating docking scores with ligand RMSD, protein flexibility, conformational sampling, and endpoint energetic analyses rather than treating these measures as interchangeable indicators of binding stability [35,36,91].

At the selected L1 surface pocket, both kanamycin C and cefiderocol underwent substantial conformational reorganisation and late-stage displacement. Although kanamycin C remained comparatively restrained during the first 80 ns, neither ligand maintained a single persistent binding geometry throughout the complete simulation. Moreover, because the investigated site is distinct from the binuclear zinc catalytic centre and the simulated receptor construct does not reproduce the native tetrameric, metal-loaded state, the L1 findings should be regarded as an exploratory alternative-site hypothesis requiring further structural and experimental validation [15,82,83].

Overall, the integrated analysis provides different levels of confidence across the investigated targets. AAC(6')-Ib4–kanamycin C represents the most coherent computationally supported complex, whereas DfrA14–cefiderocol provides the strongest dynamic comparator despite not being the top-ranked compound in the initial docking panel. DfrA14–kanamycin C remains a docking-prioritised but conformationally mobile hypothesis, while both L1 complexes require additional structural and experimental validation before stronger mechanistic conclusions can be drawn. Trimethoprim remains an important DfrA14-relevant antifolate comparator, whereas imipenem and meropenem provide the relevant carbapenem context for interpretation of the L1 docking results.

3.9 Limitations

The present study has several limitations that should be considered when interpreting the findings. The analysis relied on comparative receptor models, a single predicted binding pocket and docking-score framework for each target, and one

100-ns MD trajectory per system without independent replicates. The archived processed data included ligand RMSD for the ligand-bound complexes and protein Cα RMSD for the apo systems but did not contain holo-protein Cα RMSD; therefore, direct comparisons of protein structural stability between apo and ligand-bound states were not possible. In addition, the original SASA index selection was not retained, and SASA was consequently interpreted only as the total solvent-accessible surface area of the selected analysis group rather than as a direct measure of ligand-specific solvent burial. The selected L1 surface site also does not reproduce the native tetrameric, binuclear-metal-containing catalytic architecture, limiting mechanistic interpretation of ligand interactions at this site. Furthermore, MM/GBSA calculations were performed using 100 trajectory frames without entropy correction and were interpreted primarily for relative comparisons within each target rather than as absolute binding free energies across different proteins. This approach is consistent with established methodological considerations regarding sampling adequacy, parameter quality, uncertainty estimation, and the limited thermodynamic interpretation of single-trajectory end-state calculations [36,90,98,99]. Finally, no biochemical binding, enzyme-inhibition, bacterial-uptake, cytotoxicity, antimicrobial susceptibility, or antibiotic-potentiation experiments were performed. Therefore, computational results should be considered as testable interaction hypotheses and candidate-prioritisation evidence rather than definitive evidence of functional antibiotic repurposing or resistance-modulating activity.

4. Conclusion

This study developed and evaluated high-identity comparative models of AAC(6')-Ib4, DfrA14, and L1 from *S. maltophilia* CW002SM and systematically investigated a focused panel of antibiotics against three mechanistically distinct resistance-associated targets. Kanamycin C consistently ranked first within the docking panel for all three targets, supporting its prioritisation as the principal cross-target computational candidate. However, subsequent MD simulations revealed distinct target-dependent behaviours that were not apparent from docking alone. Kanamycin C maintained a comparatively stable binding ensemble within the acidic pocket of AAC(6')-Ib4, exhibited conformational and positional variability within the DfrA14 binding cleft, and underwent substantial late-stage displacement at the selected L1 surface pocket. Cefiderocol, in contrast, progressively reoriented within AAC(6')-Ib4, maintained a comparatively compact ligand ensemble in DfrA14, and showed substantial displacement at L1. The MM/GBSA analysis further supported charge-assisted recognition for AAC(6')-Ib4–kanamycin C and predominantly van der Waals-driven interactions for DfrA14–cefiderocol, whereas the L1 results remained exploratory because of pronounced conformational rearrangements and the non-catalytic nature of the investigated surface pocket. Overall, the integrated docking, MD, PCA, FEL, DCCM, and residue-level energy analyses provide a target-specific and mechanistically informed prioritisation of antibiotic–resistance-protein interactions, with AAC(6')-Ib4–kanamycin C emerging as the most coherent computationally supported complex. These findings provide testable hypotheses for subsequent biochemical binding and enzyme-inhibition studies, antimicrobial susceptibility and potentiation assays, and experimental evaluation of potential resistance-modulating activity in *S. maltophilia*.

Declarations

Data availability

The whole-genome sequence of *Stenotrophomonas maltophilia* CW002SM analysed in this study is available in the NCBI GenBank repository under accession number CP104863 (BioProject PRJNA876089). The nucleotide sequences of the three antibiotic-resistance genes examined, *aac(6')-Ib4*, *dfrA14*, and *blaL1*, correspond to NCBI Reference Gene Sequences NG_051844.1, NG_056035.1, and NG_047509.1, respectively. The homology models, docking outputs, MD trajectories, and MM/GBSA outputs generated during this study are available from the corresponding author upon reasonable request.

Conflict of interest

The authors declare no competing interests.

Acknowledgement

We would like to thank Universiti Malaysia Pahang Al-Sultan Abdullah for supporting this work.

Author Contributions Statement

Conceptualization: H.F.A. S.W.S & M.N.U.

Data curation: M.S.M., R.M. H.F.A. S.W.S & M.N.U.

Formal analysis: M.S.M. & R.M.

Funding acquisition: H.F.A.

Investigation: M.S.M., R.M., H.F.A. & M.N.U.

Methodology: M.S.M., R.M., H.F.A., & M.N.U.

Project administration: H.F.A. & M.N.U.

Resources: H.F.A., H.R., & M.N.U.

Software: M.N.U.

Supervision: H.F.A.

Validation: E.I. & S.W.S

Writing – original draft: M.S.M., R.M. & H.F.A.

Writing – review & editing: M.S.M., R.M., H.F.A., E.I. & M.N.U.& S.W.S

Funding

This work was supported by the UMPSA (PGRS230369) for early-stage postgraduate study.

Declaration of Generative AI and AI-assisted technologies in the writing process

During the preparation of this work, the authors used Google Gemini and Quillbot for initial brainstorming and proofread. After using this tool, the authors reviewed and edited the content as needed and take full responsibility for the content of the publication.

References

1. Antimicrobial Resistance Collaborators. Global burden of bacterial antimicrobial resistance in 2019: a systematic analysis. *Lancet Lond. Engl.* **399**, 629–655. https://doi.org/10.1016/S0140-6736(21)02724-0 (2022).
2. GBD 2021 Antimicrobial Resistance Collaborators. *Global burden of bacterial antimicrobial resistance 1990–2021: a systematic analysis with forecasts to 2050* Vol. 404, 1199–1226 (Lancet, 2024). https://doi.org/10.1016/S0140-6736(24)01867-1
3. Sati, H. et al. The WHO Bacterial Priority Pathogens List 2024: a prioritisation study to guide research, development, and public health strategies against antimicrobial resistance. *Lancet Infect. Dis.* **25**, 1033–1043.

https://doi.org/10.1016/S1473-3099(25)00118-5 (2025).

4. Butler, M. S. et al. Analysis of the Clinical Pipeline of Treatments for Drug-Resistant Bacterial Infections: Despite Progress, More Action Is Needed. *Antimicrob. Agents Chemother.* **66**, e0199121. https://doi.org/10.1128/AAC.01991-21 (2022).
5. Brooke, J. S. Advances in the Microbiology of Stenotrophomonas maltophilia. Clinical Microbiology Reviews. *Am. Soc. Microbiol.* **34** https://doi.org/10.1128/cmr.00030-19 (2021). 10.1128/cmr.00030 – 19.
6. Gil-Gil, T., Martínez, J. L. & Blanco, P. Mechanisms of antimicrobial resistance in Stenotrophomonas maltophilia: a review of current knowledge. *Expert Rev. Anti Infect. Ther.* **18**, 335–347. https://doi.org/10.1080/14787210.2020.1730178 (2020).
7. Gröschel, M. I. et al. The phylogenetic landscape and nosocomial spread of the multidrug-resistant opportunist Stenotrophomonas maltophilia. *Nat. Commun. Nat. Publishing Group.* **11**, 2044. https://doi.org/10.1038/s41467-020-15123-0 (2020).
8. Mercier-Darty, M. et al. Comparative Whole-Genome Phylogeny of Animal, Environmental, and Human Strains Confirms the Genogroup Organization and Diversity of the Stenotrophomonas maltophilia Complex. Applied and Environmental Microbiology. *Am. Soc. Microbiol.* **86**, e02919–e02919. https://doi.org/10.1128/AEM.02919-19 (2020).
9. Karakonstantis, S., Rousaki, M., Vassilopoulou, L. & Kritsotakis, E. I. Global prevalence of cefiderocol non-susceptibility in Enterobacterales, Pseudomonas aeruginosa, Acinetobacter baumannii, and Stenotrophomonas maltophilia: a systematic review and meta-analysis. *Clin. Microbiol. Infect.* **30**, 178–188. https://doi.org/10.1016/j.cmi.2023.08.029 (2024).
10. Tamma, P. D. et al. Infectious Diseases Society of America 2024 Guidance on the Treatment of Antimicrobial-Resistant Gram-Negative Infections. *Clin. Infect. Dis.* ciae403. https://doi.org/10.1093/cid/ciae403 (2024).
11. Huang, H-H., Wu, B-K., Li, L-H., Lin, Y-T. & Yang, T-C. Role of the PhoPQ two-component regulatory system in the β-lactam resistance of Stenotrophomonas maltophilia. *J. Antimicrob. Chemother.* **76**, 1480–1486. https://doi.org/10.1093/jac/dkab059 (2021).
12. Li, L-H. et al. σP-NagA-L1/L2 Regulatory Circuit Involved in ΔompA299-356-Mediated Increase in β-Lactam Susceptibility in Stenotrophomonas maltophilia. *Microbiol. Spectr.* **10**, e0279722. https://doi.org/10.1128/spectrum.02797-22 (2022).
13. Yamada, K., Ishii, Y. & Tateda, K. Diversity of blaL1-like genes in Stenotrophomonas species: insights from genome analysis of publicly available genome sequences. *Antimicrob. Agents Chemother. Am. Soc. Microbiol.* **67**, e00673–e00623. https://doi.org/10.1128/aac.00673-23 (2023).
14. Yamada, K., Ishii, Y. & Tateda, K. Biochemical characterization of the L1-like metallo-β-lactamase from Stenotrophomonas lactitubi. *Antimicrob. Agents Chemother. Am. Soc. Microbiol.* **68**, e00866–e00823. https://doi.org/10.1128/aac.00866-23 (2024).
15. Hinchliffe, P. et al. Interactions of hydrolyzed β-lactams with the L1 metallo-β-lactamase: Crystallography supports stereoselective binding of cephem/carbapenem products. *J. Biol. Chem.* **299**, 104606. https://doi.org/10.1016/j.jbc.2023.104606 (2023).
16. Gezer, Y. et al. Evaluation of clinical outcomes and risk factors associated with mortality in patients with Stenotrophomonas maltophilia bloodstream infection: a multicenter study. *BMC Infect. Dis.* **24**, 1387. https://doi.org/10.1186/s12879-024-10293-4 (2024).
17. Bostanghadiri, N. et al. Global mapping of antibiotic resistance rates among clinical isolates of Stenotrophomonas maltophilia: a systematic review and meta-analysis. *Ann. Clin. Microbiol. Antimicrob.* **23**, 26. https://doi.org/10.1186/s12941-024-00685-4 (2024).
18. Banar, M. et al. Global prevalence and antibiotic resistance in clinical isolates of Stenotrophomonas maltophilia: a systematic review and meta-analysis. *Front. Med. (Lausanne)*. **10**, 1163439.

https://doi.org/10.3389/fmed.2023.1163439 (2023).

19. Maraolo, A. E. et al. *Stenotrophomonas maltophilia Infections: A Systematic Review and Meta-Analysis of Comparative Efficacy of Available Treatments, with Critical Assessment of Novel Therapeutic Options. Antibiotics* Vol. 12, 910 (Multidisciplinary Digital Publishing Institute, 2023). https://doi.org/10.3390/antibiotics12050910
20. Almangour, T. A. et al. Trimethoprim-sulfamethoxazole versus levofloxacin for the treatment of Stenotrophomonas maltophilia infections: A multicentre cohort study. *J. Glob Antimicrob. Resist.* **38**, 42–48. https://doi.org/10.1016/j.jgar.2024.05.016 (2024).
21. Almangour, T. A. et al. Monotherapy versus combination for the treatment of Stenotrophomonas maltophilia: a multicenter cohort study. *Expert Rev. Anti Infect. Ther.* **22**, 997–1005. https://doi.org/10.1080/14787210.2024.2353704 (2024).
22. d'Udekem d'Acoz, O. et al. Dynamics and quantitative contribution of the aminoglycoside 6'-N-acetyltransferase type Ib to amikacin resistance. mSphere. *Am. Soc. Microbiol.* **9**, e00789–e00723. https://doi.org/10.1128/msphere.00789-23 (2024).
23. Ahmed, S. et al. Retention of antibiotic activity against resistant bacteria harbouring aminoglycoside-N-acetyltransferase enzyme by adjuvants: a combination of in-silico and in-vitro study. *Sci. Rep. Nat. Publishing Group.* **10**, 19381. https://doi.org/10.1038/s41598-020-76355-0 (2020).
24. El-Khoury, C. et al. The role of adjuvants in overcoming antibacterial resistance due to enzymatic drug modification. *RSC Med. Chem.* **13**, 1276–1299. https://doi.org/10.1039/d2md00263a (2022).
25. Revillo Imbernon, J., Weibel, J-M., Ennifar, E., Prévost, G. & Kellenberger, E. Structural analysis of neomycin B and kanamycin A binding Aminoglycosides Modifying Enzymes (AME) and bacterial ribosomal RNA. *Mol. Inf.* **43**, e202300339. https://doi.org/10.1002/minf.202300339 (2024).
26. Rocha, K. et al. *Inhibition of Aminoglycoside 6'-N-acetyltransferase Type Ib (AAC(6')-Ib): Structure–Activity Relationship of Substituted Pyrrolidine Pentamine Derivatives as Inhibitors. Biomedicines* Vol. 9, 1218 (Multidisciplinary Digital Publishing Institute, 2021). https://doi.org/10.3390/biomedicines9091218
27. Sklenicka, J. et al. Structure–Activity Relationship of Pyrrolidine Pentamine Derivatives as Inhibitors of the Aminoglycoside 6'-N-Acetyltransferase Type Ib. *Antibiot. Multidisciplinary Digit. Publishing Inst.* **13**, 672. https://doi.org/10.3390/antibiotics13070672 (2024).
28. Sánchez-Osuna, M., Cortés, P., Llagostera, M., Barbé, J. & Erill, I. Exploration into the origins and mobilization of di-hydrofolate reductase genes and the emergence of clinical resistance to trimethoprim. *Microb. Genomics Microbiol. Soc.* **6**, e000440. https://doi.org/10.1099/mgen.0.000440 (2020).
29. Ambrose, S. J. & Hall, R. M. dfrA trimethoprim resistance genes found in Gram-negative bacteria: compilation and unambiguous numbering. *J. Antimicrob. Chemother.* **76**, 2748–2756. https://doi.org/10.1093/jac/dkab212 (2021).
30. Krucinska, J. et al. Structure-guided functional studies of plasmid-encoded dihydrofolate reductases reveal a common mechanism of trimethoprim resistance in Gram-negative pathogens. *Commun. Biol.* **5**, 459. https://doi.org/10.1038/s42003-022-03384-y (2022).
31. Li, L. et al. Identification and characterization of two novel ISCR1-associated genes dfrA42 and dfrA43 encoding trimethoprim resistant dihydrofolate reductases. Antimicrob Agents Chemother. ;95:e02010-20, AAC.02010-20. (2023). https://doi.org/10.1128/AAC.02010-20
32. Ambrose, S. J. & Hall, R. M. Origin of the dfrA44 trimethoprim resistance gene. *J. Antimicrob. Chemother.* **76**, 3312–3314. https://doi.org/10.1093/jac/dkab330 (2021).
33. Vetting, M. W. et al. Mechanistic and Structural Analysis of Aminoglycoside N-Acetyltransferase AAC(6')-Ib and Its Bifunctional, Fluoroquinolone-Active AAC(6')-Ib-cr Variant. [cited 2026 Aug 2]; (2008). https://dx.doi.org/10.1021/bi800664x. Accessed 2 Aug 2026.

34. Biagi, M. et al. Activity of Cefiderocol Alone and in Combination with Levofloxacin, Minocycline, Polymyxin B, or Trimethoprim-Sulfamethoxazole against Multidrug-Resistant Stenotrophomonas maltophilia. *Antimicrob. Agents Chemother.* **64**, e00559–e00520. https://doi.org/10.1128/AAC.00559-20 (2020).
35. Bender, B. J. et al. A practical guide to large-scale docking. *Nat. Protoc.* **16**, 4799–4832. https://doi.org/10.1038/s41596-021-00597-z (2021).
36. Valdés-Tresanco, M. S., Valdés-Tresanco, M. E., Valiente, P. A., Moreno, E. & gmx_MMPBSA: A New Tool to Perform End-State Free Energy Calculations with GROMACS. *J. Chem. Theory Comput.* **17**, 6281–6291. https://doi.org/10.1021/acs.jctc.1c00645 (2021).
37. Wang, E. et al. Development and Evaluation of MM/GBSA Based on a Variable Dielectric GB Model for Predicting Protein–Ligand Binding Affinities. [cited 2026 July 31]; (2020). https://dx.doi.org/10.1021/acs.jcim.0c00024. Accessed 31 July 2026.
38. Waterhouse, A. et al. SWISS-MODEL: homology modelling of protein structures and complexes. *Nucleic Acids Res.* **46**, W296–303. https://doi.org/10.1093/nar/gky427 (2018).
39. Studer, G. et al. QMEANDisCo-distance constraints applied on model quality estimation. *Bioinf. Oxf. Engl.* **36**, 1765–1771. https://doi.org/10.1093/bioinformatics/btz828 (2020).
40. Laskowski, R. A., MacArthur, M. W., Moss, D. S. & Thornton, J. M. PROCHECK: a program to check the stereochemical quality of protein structures. *J. Appl. Crystallogr.* **26**, 283–291. https://doi.org/10.1107/S0021889892009944 (1993).
41. Colovos, C. & Yeates, T. O. Verification of protein structures: Patterns of nonbonded atomic interactions. *Protein Sci.* **2**, 1511–1519. https://doi.org/10.1002/pro.5560020916 (1993).
42. Eisenberg, D., Lüthy, R. & Bowie, J. U. VERIFY3D: assessment of protein models with three-dimensional profiles. *Methods Enzymol.* **277**, 396–404. https://doi.org/10.1016/s0076-6879(97)77022-8 (1997).
43. Polák, L. et al. PrankWeb 4: a modular web server for protein-ligand binding site prediction and downstream analysis. *Nucleic Acids Res.* **53**, W466–W471. https://doi.org/10.1093/nar/gkaf421 (2025).
44. Sastry, G. M., Adzhigirey, M., Day, T., Annabhimoju, R. & Sherman, W. Protein and ligand preparation: parameters, protocols, and influence on virtual screening enrichments. *J. Comput. Aided Mol. Des.* **27**, 221–234. https://doi.org/10.1007/s10822-013-9644-8 (2013).
45. Roos, K. et al. OPLS3e: Extending Force Field Coverage for Drug-Like Small Molecules. *J. Chem. Theory Comput. Am. Chem. Soc.* **15**, 1863–1874. https://doi.org/10.1021/acs.jctc.8b01026 (2019).
46. Schrödinger, L. L. C. *LigPrep, version 3.1* (Schrödinger, LLC, 2014).
47. Shelley, J. C. et al. Epik: a software program for pK(a) prediction and protonation state generation for drug-like molecules. *J. Comput. Aided Mol. Des.* **21**, 681–691. https://doi.org/10.1007/s10822-007-9133-z (2007).
48. Friesner, R. A. et al. Glide: a new approach for rapid, accurate docking and scoring. 1. Method and assessment of docking accuracy. *J. Med. Chem.* **47**, 1739–1749. https://doi.org/10.1021/jm0306430 (2004).
49. Friesner, R. A. et al. Extra Precision Glide: Docking and Scoring Incorporating a Model of Hydrophobic Enclosure for Protein–Ligand Complexes. *J. Med. Chem. Am. Chem. Soc.* **49**, 6177–6196. https://doi.org/10.1021/jm051256o (2006).
50. Abraham, M. J. et al. GROMACS: High performance molecular simulations through multi-level parallelism from laptops to supercomputers. *SoftwareX* **1–2**, 19–25. https://doi.org/10.1016/j.softx.2015.06.001 (2015).
51. MacKerell, A. D. et al. All-Atom Empirical Potential for Molecular Modeling and Dynamics Studies of Proteins†. 1998 [cited 2026 July 31]; https://dx.doi.org/10.1021/jp973084f. Accessed 31 July 2026.
52. Vanommeslaeghe, K. et al. CHARMM general force field: A force field for drug-like molecules compatible with the CHARMM all-atom additive biological force fields. *J. Comput. Chem.* **31**, 671–690. https://doi.org/10.1002/jcc.21367 (2010).

53. Vanommeslaeghe, K., Raman, E. P. & MacKerell, A. D. Automation of the CHARMM General Force Field (CGenFF) II: Assignment of Bonded Parameters and Partial Atomic Charges. [cited 2026 Aug 2]; (2012). https://dx.doi.org/10.1021/ci3003649. Accessed 2 Aug 2026.
54. Jorgensen, W. L., Chandrasekhar, J., Madura, J. D., Impey, R. W. & Klein, M. L. Comparison of simple potential functions for simulating liquid water. *J. Chem. Phys.* **79**, 926–935. https://doi.org/10.1063/1.445869 (1983).
55. Amadei, A., Linssen, A. B. M. & Berendsen, H. J. C. Essential dynamics of proteins. *Proteins Struct. Funct. Bioinform.* **17**, 412–425. https://doi.org/10.1002/prot.340170408 (1993).
56. Papaleo, E., Mereghetti, P., Fantucci, P., Grandori, R. & De Gioia, L. Free-energy landscape, principal component analysis, and structural clustering to identify representative conformations from molecular dynamics simulations: The myoglobin case. *J. Mol. Graph. Model.* **27**, 889–899. https://doi.org/10.1016/j.jmgm.2009.01.006 (2009).
57. Miller, B. R. et al. MMPBSA.py: An Efficient Program for End-State Free Energy Calculations. *J. Chem. Theory Comput. Am. Chem. Soc.* **8**, 3314–3321. https://doi.org/10.1021/ct300418h (2012).
58. Onufriev, A., Bashford, D. & Case, D. A. Exploring protein native states and large-scale conformational changes with a modified generalized born model. *Proteins Struct. Funct. Bioinform.* **55**, 383–394. https://doi.org/10.1002/prot.20033 (2004).
59. Muhammed, M. T. & Aki-Yalcin, E. Homology modeling in drug discovery: Overview, current applications, and future perspectives. *Chem. Biol. Drug Des.* **93**, 12–20. https://doi.org/10.1111/cbdd.13388 (2019).
60. Cavasotto, C. N. & Phatak, S. S. Homology modeling in drug discovery: current trends and applications. *Drug Discov Today*. **14**, 676–683. https://doi.org/10.1016/j.drudis.2009.04.006 (2009).
61. Cavasotto, C. N. Homology models in docking and high-throughput docking. *Curr. Top. Med. Chem.* **11**, 1528–1534. https://doi.org/10.2174/156802611795860951 (2011).
62. Cain, R., Narramore, S., McPhillie, M., Simmons, K. & Fishwick, C. W. G. Applications of structure-based design to antibacterial drug discovery. *Bioorg. Chem.* **55**, 69–76. https://doi.org/10.1016/j.bioorg.2014.05.008 (2014).
63. Finn, J. Application of SBDD to the discovery of new antibacterial drugs. *Methods Mol. Biol. Clifton N J.* **841**, 291–319. https://doi.org/10.1007/978-1-61779-520-6_13 (2012).
64. Kitchen, D. B., Decornez, H., Furr, J. R. & Bajorath, J. Docking and scoring in virtual screening for drug discovery: methods and applications. *Nat. Rev. Drug Discov*. **3**, 935–949. https://doi.org/10.1038/nrd1549 (2004).
65. Meng, X-Y., Zhang, H-X., Mezei, M. & Cui, M. Molecular docking: a powerful approach for structure-based drug discovery. *Curr. Comput. Aided Drug Des.* **7**, 146–157. https://doi.org/10.2174/157340911795677602 (2011).
66. Lionta, E., Spyrou, G., Vassilatis, D. K. & Cournia, Z. Structure-based virtual screening for drug discovery: principles, applications and recent advances. *Curr. Top. Med. Chem.* **14**, 1923–1938. https://doi.org/10.2174/1568026614666140929124445 (2014).
67. Grinter, S. Z. & Zou, X. Challenges, applications, and recent advances of protein-ligand docking in structure-based drug design. *Molecules Basel Switz.* **19**, 10150–10176. https://doi.org/10.3390/molecules190710150 (2014).
68. Forli, S. et al. Computational protein–ligand docking and virtual drug screening with the AutoDock suite. *Nat. Protoc. Nat. Publishing Group.* **11**, 905–919. https://doi.org/10.1038/nprot.2016.051 (2016).
69. Zhu, H., Zhang, Y., Li, W. & Huang, N. A Comprehensive Survey of Prospective Structure-Based Virtual Screening for Early Drug Discovery in the Past Fifteen Years. *Int. J. Mol. Sci.* **23**, 15961. https://doi.org/10.3390/ijms232415961 (2022).
70. Xu, X. & Zou, X. Docking-based virtual screening: Past, present, and future. *Biophys. J. [Internet]*. https://doi.org/10.1016/j.bpj.2026.04.011 (2026). [cited 2026 Aug 9].
71. Chiem, K. et al. Identification of an Inhibitor of the Aminoglycoside 6'-N-Acetyltransferase type Ib [AAC(6')-Ib] by Glide Molecular Docking. *Medchemcomm* **7**, 184–189. https://doi.org/10.1039/C5MD00316D (2016).

72. Sreenithya, K. H., Manoharadas, S. & Sugumar, S. Comprehensive screening of potential inhibitors from ZINC15 database for Metallo-L1 B -Lactamase from Stenotrophomonas maltophilia via in Silico and in vitro approaches. *BMC Microbiol.* **25**, 268. https://doi.org/10.1186/s12866-025-03994-6 (2025).
73. Liu, X. et al. Molecular dynamics simulations and novel drug discovery. *Expert Opin. Drug Discov*. **13**, 23–37. https://doi.org/10.1080/17460441.2018.1403419 (2018).
74. Wei, H. & McCammon, J. A. Structure and dynamics in drug discovery. npj Drug Discov. *Nat. Publishing Group.* **1**, 1. https://doi.org/10.1038/s44386-024-00001-2 (2024).
75. Grewal, S., Deswal, G., Grewal, A. S. & Guarve, K. Molecular dynamics simulations: Insights into protein and protein ligand interactions. *Adv. Pharmacol. San Diego Calif.* **103**, 139–162. https://doi.org/10.1016/bs.apha.2025.01.007 (2025).
76. AlRawashdeh, S. & Barakat, K. H. Applications of Molecular Dynamics Simulations in Drug Discovery. *Methods Mol. Biol. Clifton N J.* **2714**, 127–141. https://doi.org/10.1007/978-1-0716-3441-7_7 (2024).
77. Dubey, K. D., Tiwari, R. K. & Ojha, R. P. Recent advances in protein-ligand interactions: molecular dynamics simulations and binding free energy. *Curr. Comput. Aided Drug Des.* **9**, 518–531. https://doi.org/10.2174/15734099113096660036 (2013).
78. Fu, H. et al. Accurate determination of protein:ligand standard binding free energies from molecular dynamics simulations. *Nat. Protoc.* **17**, 1114–1141. https://doi.org/10.1038/s41596-021-00676-1 (2022).
79. Naqvi, A. A. T., Mohammad, T., Hasan, G. M. & Hassan, M. I. Advancements in Docking and Molecular Dynamics Simulations Towards Ligand-receptor Interactions and Structure-function Relationships. *Curr. Top. Med. Chem.* **18**, 1755–1768. https://doi.org/10.2174/1568026618666181025114157 (2018).
80. Mortier, J. et al. The impact of molecular dynamics on drug design: applications for the characterization of ligand-macromolecule complexes. *Drug Discov Today*. **20**, 686–702. https://doi.org/10.1016/j.drudis.2015.01.003 (2015).
81. Muteeb, G., Alsultan, A., Farhan, M. & Aatif, M. Risedronate and Methotrexate Are High-Affinity Inhibitors of New Delhi Metallo-β-Lactamase-1 (NDM-1): A Drug Repurposing Approach. *Molecules Multidisciplinary Digit. Publishing Inst.* **27**, 1283. https://doi.org/10.3390/molecules27041283 (2022).
82. Wilamowski, M. et al. Time-resolved β-lactam cleavage by L1 metallo-β-lactamase. *Nat. Commun.* **13**, 7379. https://doi.org/10.1038/s41467-022-35029-3 (2022).
83. Kim, Y. et al. Structural and biochemical analysis of the metallo-β-lactamase L1 from emerging pathogen Stenotrophomonas maltophilia revealed the subtle but distinct di-metal scaffold for catalytic activity. *Protein Sci.* **29**, 723–743. https://doi.org/10.1002/pro.3804 (2020).
84. Stein, S., Loccisano, A., Firestine, S. & Evanseck, J. Principal Components Analysis: A Review of its Application on Molecular Dynamics Data. Annual Reports in Computational Chemistry. ;2:233–61. (2006). https://doi.org/10.1016/S1574-1400(06)02013-5
85. Alanazi, A. et al. A combined in silico and MD simulation approach to discover novel LpxC inhibitors targeting multiple drug resistant Pseudomonas aeruginosa. *Sci. Rep. Nat. Publishing Group.* **15**, 16900. https://doi.org/10.1038/s41598-025-99215-1 (2025).
86. Gul, F., Parvaiz, N. & Azam, S. S. Deciphering the relational dynamics of AF-2 domain of PAN PPAR through drug repurposing and comparative simulations. *PLOS ONE Public. Libr. Sci.* **18**, e0283743. https://doi.org/10.1371/journal.pone.0283743 (2023).
87. Yu, H. & Dalby, P. A. A beginner's guide to molecular dynamics simulations and the identification of cross-correlation networks for enzyme engineering. *Methods Enzymol.* **643**, 15–49. https://doi.org/10.1016/bs.mie.2020.04.020 (2020).
88. Muthukumar, T. et al. Transcriptomics-guided discovery of Interleukin-6 modulators from Bacillus subtilis metabolites in type 2 diabetes mellitus. *Front. Bioinform [Internet] Front.* https://doi.org/10.3389/fbinf.2026.1792877 (2026). [cited

2026 Aug 9];6.

89. Kumari, M., Singh, R. & Subbarao, N. Exploring the interaction mechanism between potential inhibitor and multi-target Mur enzymes of mycobacterium tuberculosis using molecular docking, molecular dynamics simulation, principal component analysis, free energy landscape, dynamic cross-correlation matrices, vector movements, and binding free energy calculation. *J. Biomol. Struct. Dyn.* **40**, 13497–13526. https://doi.org/10.1080/07391102.2021.1989040 (2022).
90. Wang, E. et al. End-Point Binding Free Energy Calculation with MM/PBSA and MM/GBSA: Strategies and Applications in Drug Design. *Chem. Rev. Am. Chem. Soc.* **119**, 9478–9508. https://doi.org/10.1021/acs.chemrev.9b00055 (2019).
91. Genheden, S. & Ryde, U. The MM/PBSA and MM/GBSA methods to estimate ligand-binding affinities. *Expert Opin. Drug Discovery Taylor Francis*. **10**, 449–461. https://doi.org/10.1517/17460441.2015.1032936 (2015).
92. Decherchi, S. & Cavalli, A. Thermodynamics and Kinetics of Drug-Target Binding by Molecular Simulation. *Chem. Rev.* **120**, 12788–12833. https://doi.org/10.1021/acs.chemrev.0c00534 (2020).
93. Hou, T., Wang, J., Li, Y. & Wang, W. Assessing the performance of the MM/PBSA and MM/GBSA methods. 1. The accuracy of binding free energy calculations based on molecular dynamics simulations. *J. Chem. Inf. Model.* **51**, 69–82. https://doi.org/10.1021/ci100275a (2011).
94. Adediwura, V. A., Koirala, K., Do, H. N., Wang, J. & Miao, Y. Understanding the impact of binding free energy and kinetics calculations in modern drug discovery. *Expert Opin. Drug Discov*. **19**, 671–682. https://doi.org/10.1080/17460441.2024.2349149 (2024).
95. Yu, Y. X. et al. Decoding molecular mechanism underlying binding of drugs to HIV-1 protease with molecular dynamics simulations and MM-GBSA calculations. *SAR QSAR Environ. Res.* **32**, 889–915. https://doi.org/10.1080/1062936X.2021.1979647 (2021).
96. Romanowicz, K. J., Resnick, C., Hinton, S. R. & Plesa, C. Exploring antibiotic resistance in diverse homologs of the dihydrofolate reductase protein family through broad mutational scanning. *Sci. Adv. Am. Association Advancement Sci.* **11**, eadw9178. https://doi.org/10.1126/sciadv.adw9178 (2025).
97. Su, M. et al. Comparative Assessment of Scoring Functions: The CASF-2016 Update. *J. Chem. Inf. Model. Am. Chem. Soc.* **59**, 895–913. https://doi.org/10.1021/acs.jcim.8b00545 (2019).
98. Wan, S., Sinclair, R. C. & Coveney, P. V. Uncertainty quantification in classical molecular dynamics. *Phil Trans. R Soc. A*. **379**, 20200082. https://doi.org/10.1098/rsta.2020.0082 (2021).
99. Xu, X. et al. Sampling Challenges of MM/PBSA Binding Energy Calculations. *J. Phys. Chem. B Am. Chem. Soc.* **129**, 11666–11678. https://doi.org/10.1021/acs.jpcb.5c04908 (2025).

Tables

Table 1. Targets, genes, CDS lengths, protein lengths, templates, resolution, sequence identity, and downstream receptor state.

Target	Gene	CDS length (bp)	Protein length (aa)	Template (PDB, chain)	Template resolution (Å)	Sequence identity (%)	Downstream receptor state
AAC(6')-Ib4	aac(6')-Ib4	555	179	2BUE, A	1.70	98.48	Monomer
DfrA14	dfrA14	474	157	7R6G, A	2.61	89.81	Monomer (template is a homodimer)
L1 metallo-β-lactamase	blaL1	873	267	6UAF, A	1.90	98.97	Single chain A

Table 2. GMQE, QMEANDisCo, ERRAT, Ramachandran categories, and Verify3D.

Target	GMQE	QMEANDisCo	ERRAT quality factor	Ramachandran preferred (%)	Ramachandran allowed (%)	Ramachandran outliers (%)	Verify3D
AAC(6')-Ib4	0.84	0.87	96.364	98.87	1.13	0.00	91.62% ≥ 0.1 averaged 3D–1D score
DfrA14	0.91	0.88	84.173	92.26	7.10	0.65	No unambiguous overall percentage recoverable
L1 chain A	0.92	0.91	92.948	95.66	3.58	0.75	No unambiguous overall percentage recoverable

Table 3. P2Rank coordinates, scores, probabilities, and principal residues.

Target	Pocket centre x (Å)	y (Å)	z (Å)	P2Rank score	Probability	Principal predicted residues
AAC(6')-Ib4	12.356	6.502	15.909	52.01	0.979	Gln75, Gln102, Tyr104, Ser109, Trp113, Asp126, Asp163, Asn168, Asp190
DfrA14	16.255	−27.561	5.941	66.29	0.989	Met9, Ala10, Ala11, Ile18, Trp26, Glu31, Gln32, Phe35, Thr50, Met54, Leu57, Ser100, Gly102, Tyr106
L1 chain A	26.209	45.395	−4.206	17.74	0.806	Asn128, Ala129, Glu130, Asp162, Phe177, Pro179, Pro183, Tyr220, Arg222, Asp226, Arg229

Table 4. Docking scores and within-target ranks for the focused score-ranked antibiotic panel. Cefiderocol was docked separately for MD pose generation and was not included in the archived score-ranked files.

Antibiotic	AAC(6')-Ib4 score (rank)	DfrA14 score (rank)	L1 score (rank)	Mean rank
Kanamycin C	−8.856 (1)	−7.719 (1)	−5.678 (1)	1.00
Imipenem	−7.159 (2)	−6.900 (4)	−5.524 (2)	2.67
Meropenem	−5.798 (4)	−7.493 (2)	−4.086 (3)	3.00
Trimethoprim	−5.888 (3)	−7.347 (3)	−3.930 (4)	3.33

Table 5. MD summary. Complex RMSD values are ligand heavy-atom RMSD after protein fitting; apo RMSD values are protein Cα RMSD and are listed as a separate observable. SASA is reported as the total solvent-accessible area of the

archived selected analysis group.

System	RMSD (nm; complexes: ligand RMSD; apo: protein Cα RMSD)	Protein RMSF (nm)	Rg (nm)	Selected-group SASA (nm²)	H-bond trend
AAC(6')-Ib4–kanamycin C	0.160 ± 0.040	0.119	1.578 ± 0.009	99.31 ± 1.82	Generally 4–9
AAC(6')-Ib4–cefiderocol	0.552 ± 0.173	0.127	1.605 ± 0.010	102.27 ± 2.17	Early loss; later ~3–6
Apo AAC(6')-Ib4	0.173 ± 0.020	0.095	1.589 ± 0.011	103.91 ± 1.89	n/a
DfrA14–kanamycin C	0.677 ± 0.160	0.134	1.567 ± 0.010	91.62 ± 1.80	Mostly 2–5; lower late
DfrA14–cefiderocol	0.174 ± 0.036	0.116	1.542 ± 0.008	87.73 ± 1.71	Generally 1–5
Apo DfrA14	0.143 ± 0.020	0.086	1.520 ± 0.008	91.46 ± 1.59	n/a
L1–kanamycin C	1.467 ± 1.650	0.880	2.849 ± 0.331	238.08 ± 2.99	~2–4 early; ~4–7 later
L1–cefiderocol	2.185 ± 1.190	1.431	2.956 ± 0.641	236.27 ± 4.70	Sparse early; ~2–5 later
Apo L1	1.066 ± 1.240	1.420	2.948 ± 0.647	233.29 ± 4.16	n/a

Table 6. MM/GBSA energy components and total values (kcal/mol).

Complex	ΔEvdW	ΔEelectrostatic	ΔGGB	ΔGESURF	ΔGtotal
AAC(6')-Ib4–kanamycin C	−23.14	−1657.96	+1608.60	−5.81	−78.31 ± 9.55
AAC(6')-Ib4–cefiderocol	−49.09	−385.54	+429.13	−6.70	−12.21 ± 8.78
DfrA14–kanamycin C	−14.73	−319.61	+322.58	−3.67	−15.43 ± 8.18
DfrA14–cefiderocol	−70.63	−92.17	+146.59	−9.05	−25.25 ± 5.06
L1–kanamycin C	−7.38	−611.37	+598.02	−2.42	−23.16 ± 12.01
L1–cefiderocol	−25.61	−126.85	+143.34	−3.65	−12.77 ± 5.61

Table 7. Selected per-residue MM/GBSA energetic contributors.

Complex	Principal favourable per-residue contributors (kcal/mol, selected)
AAC(6')-Ib4–kanamycin C	Asp163 −28.68; Asp126 −18.82; Trp113 −6.87; also Glu64, Tyr104, Gln75, Asp190, Pro164
AAC(6')-Ib4–cefiderocol	Asp163 +4.01; Asp126 +2.91 (net unfavourable); favourable: Trp60, Tyr104, Trp113, Gly61, Gly62, Ser109, Pro164
DfrA14–cefiderocol	Met54 −5.21; Phe35 −3.88; Leu57 −2.46; Ile18 −2.46; Thr50 −2.03; Gln32 −1.83; Ser100 −1.72
DfrA14–kanamycin C	Favourable contributors: Ser53, Ile24, Trp26, Pro22, Asp23, Ala28, Met54, Gly21
L1–kanamycin C	Favourable contributors: Asp226, Glu225, Glu130, Pro221
L1–cefiderocol	Favourable contributors: Leu143, Arg219, Pro218, Asn141, Asp142, Tyr220

Figures

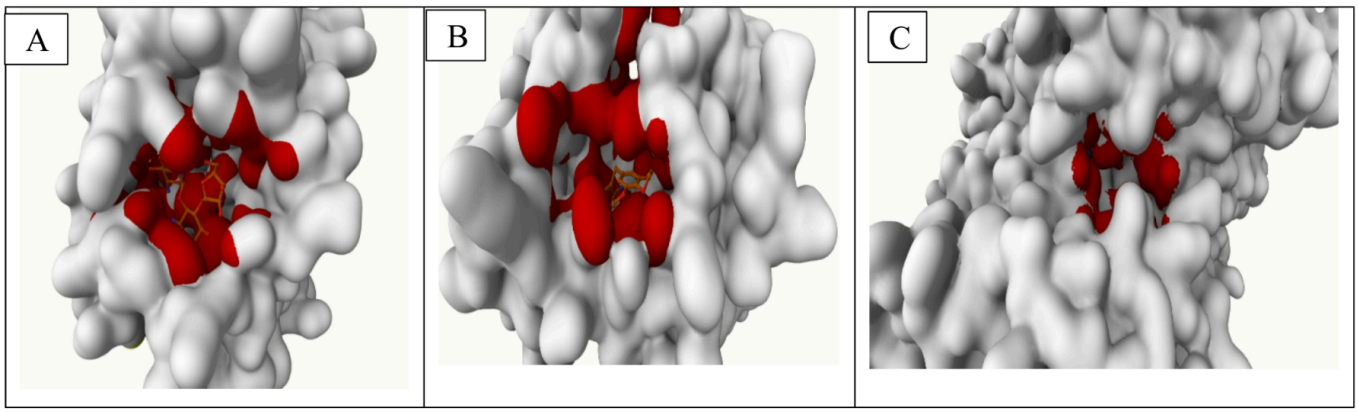


Figure 1

Comparative structural models and principal P2Rank/PrankWeb-predicted pockets for (A) AAC(6')-Ib4, (B) DfrA14, and (C) L1 chain A.

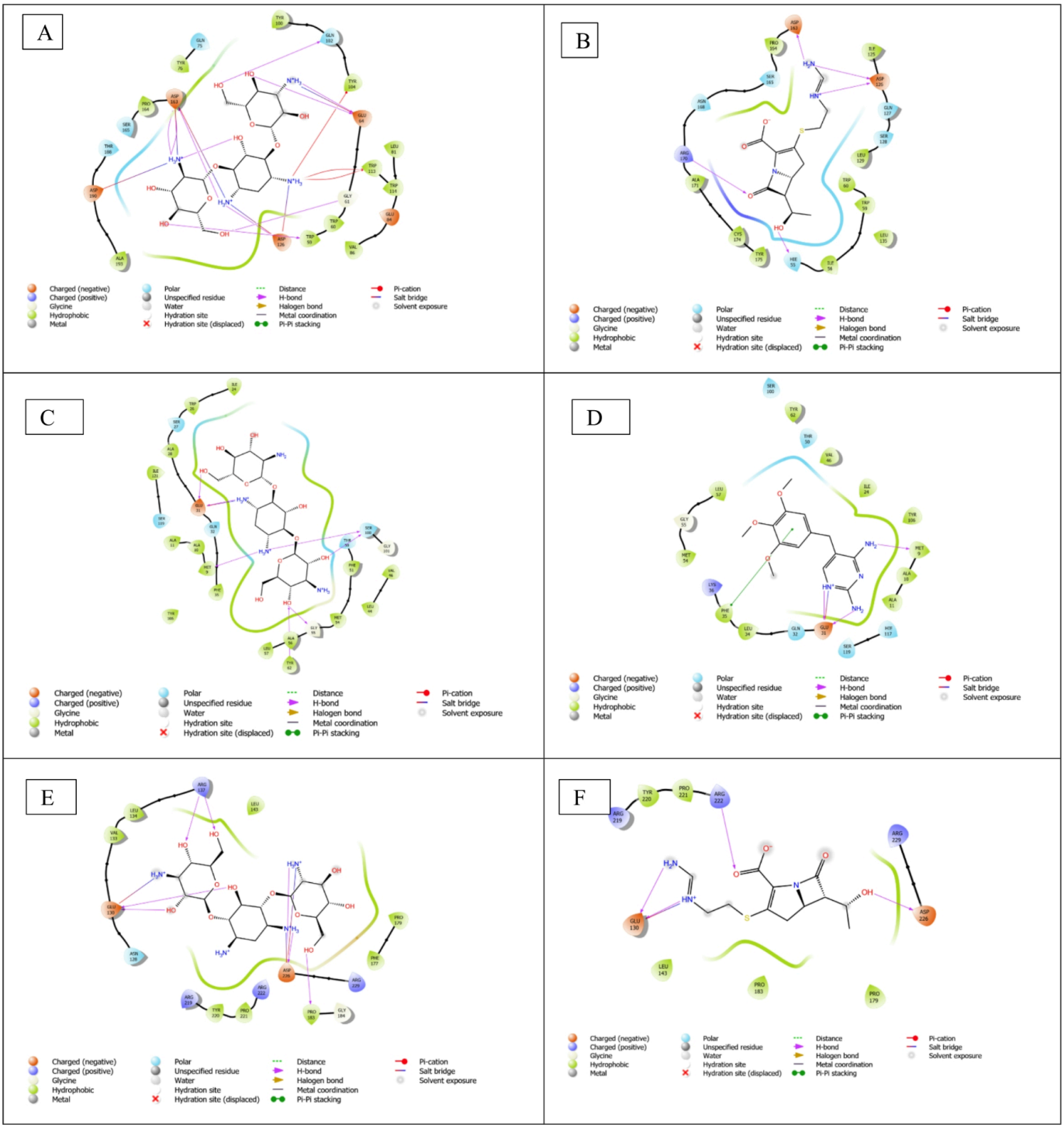


Figure 2

Representative two-dimensional docking interaction diagrams from the focused antibiotic panel: (A) AAC(6')-Ib4–kanamycin C, (B) AAC(6')-Ib4–imipenem, (C) DfrA14–kanamycin C, (D) DfrA14–trimethoprim, (E) L1–kanamycin C, and (F) L1–imipenem. Additional interaction maps for all five selected antibiotics are provided in Supplementary Figures S6–S8.

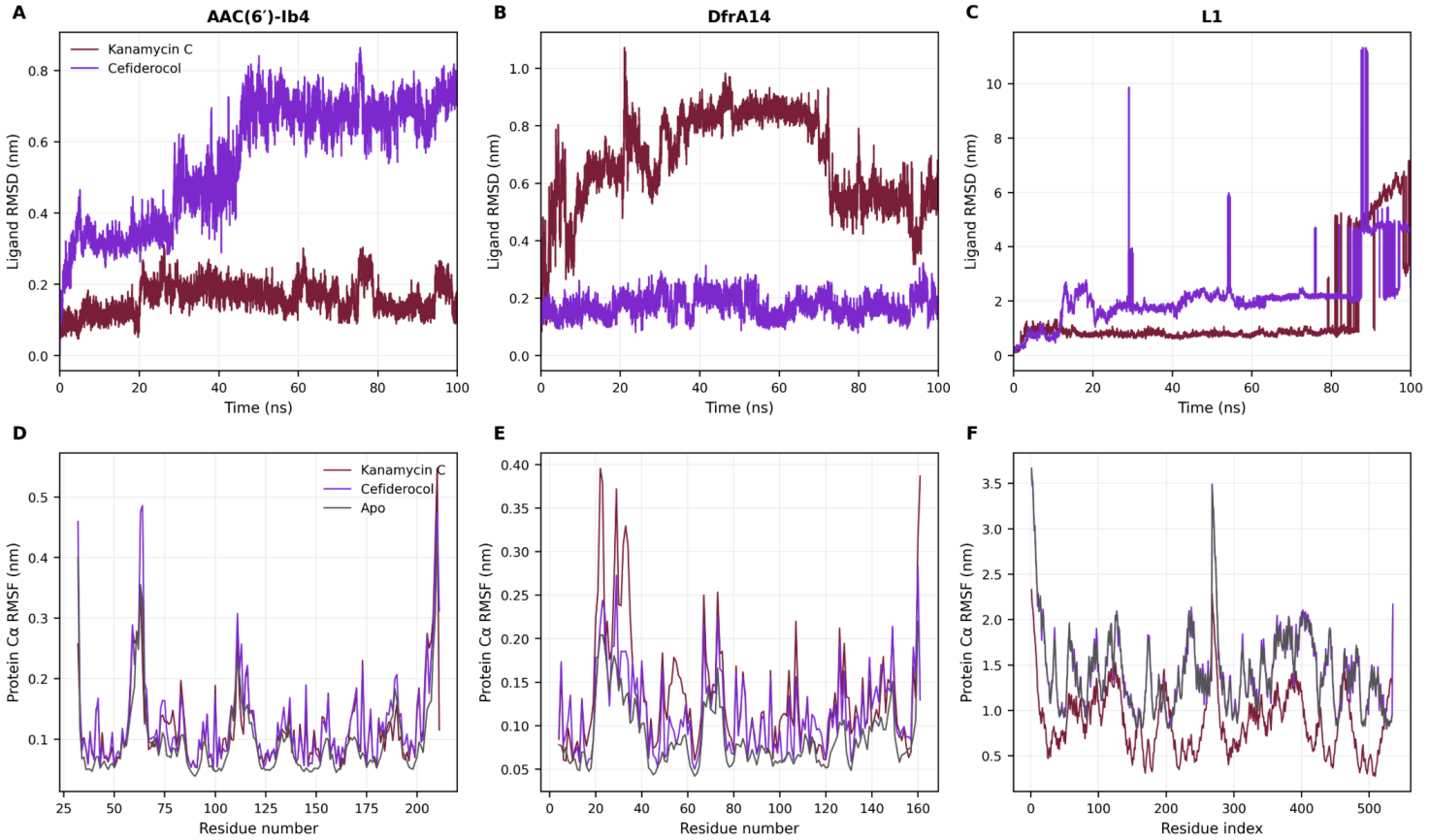


Figure 3

Time-resolved ligand positional behaviour and protein flexibility. (A–C) Ligand heavy-atom RMSD after protein fitting for kanamycin C and cefiderocol in AAC(6')-Ib4, DfrA14, and L1, respectively. (D–F) Protein Cα RMSF profiles for the corresponding kanamycin C-bound, cefiderocol-bound, and apo trajectories. Apo-protein Cα RMSD is presented separately in Supplementary Figure S2 and is not directly compared with ligand RMSD.

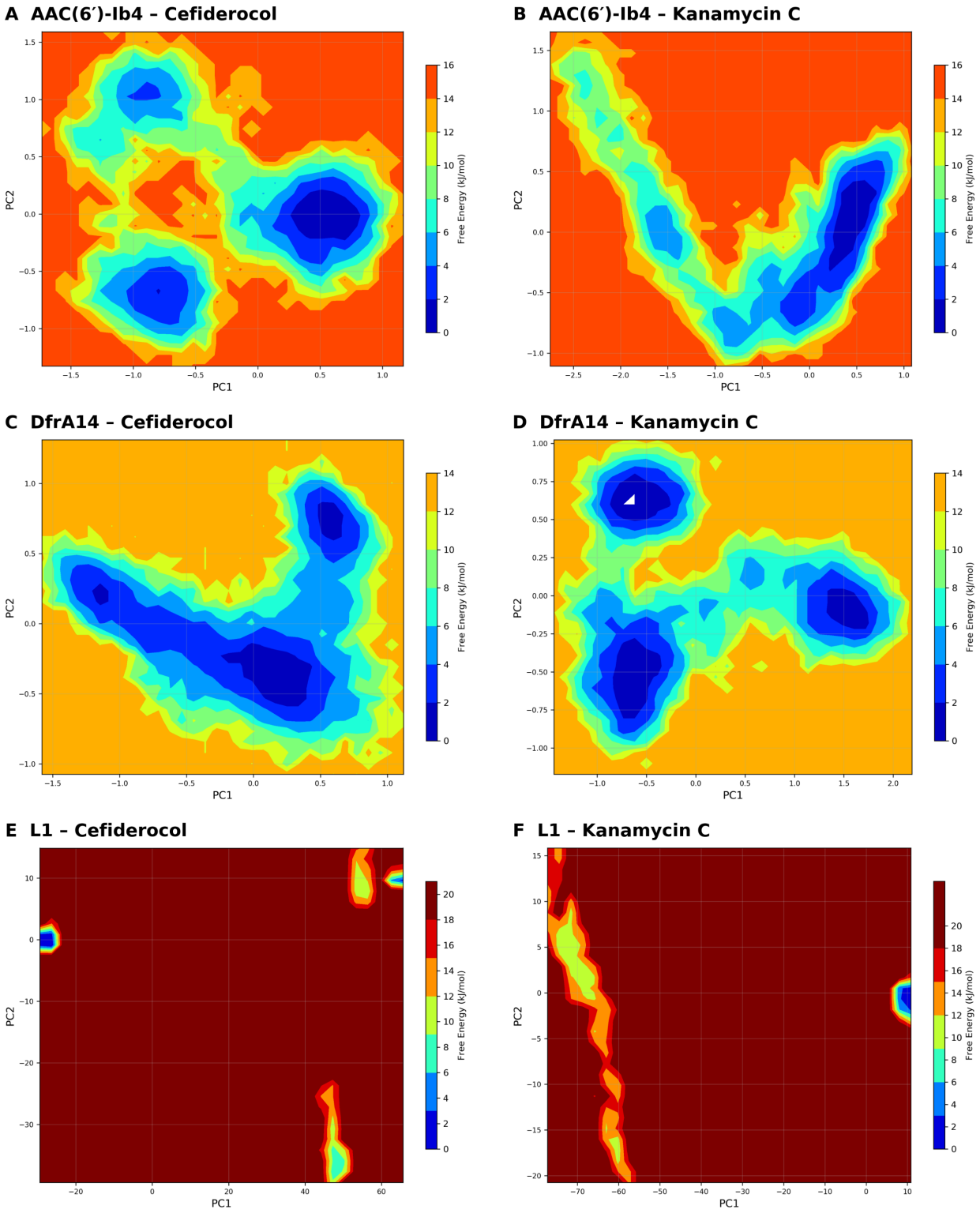


Figure 4

Two-dimensional free-energy landscapes projected onto PC1 and PC2 for (A) AAC(6')-Ib4–cefiderocol, (B) AAC(6')-Ib4–kanamycin C, (C) DfrA14–cefiderocol, (D) DfrA14–kanamycin C, (E) L1–cefiderocol, and (F) L1–kanamycin C. Lower-energy, more populated regions are shown in blue. Because each system was represented by one trajectory, basin number and connectivity are interpreted descriptively rather than as converged thermodynamic properties.

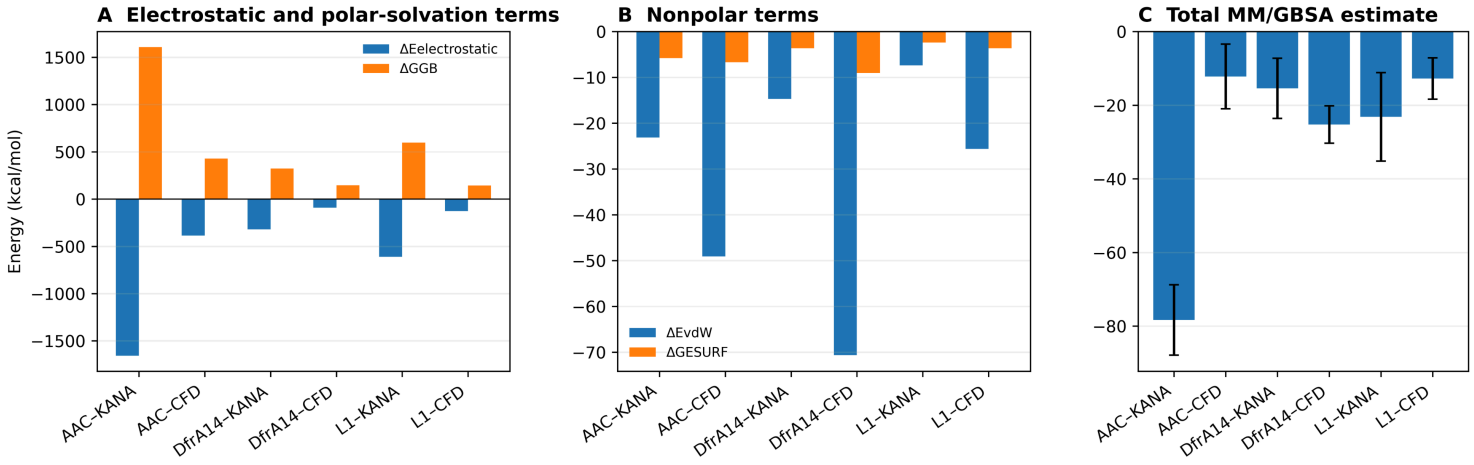


Figure 5

MM/GBSA energy decomposition for the six ligand-bound systems. (A) Electrostatic interaction and polar-solvation terms, (B) van der Waals and nonpolar-solvation terms, and (C) total MM/GBSA estimates with standard-deviation error bars. KANA, kanamycin C; CFD, cefiderocol. Values are comparative end-state estimates and are not experimental binding free energies.